

Effective-medium theory for infinite-contrast, 2D-periodic, linear composites with strongly anisotropic matrix behavior: dilute limit and cross-over behavior

François Willot,^{1,*} Yves-Patrick Pellegrini,^{1,†} Martín I. Idiart,^{2,3,‡} and Pedro Ponte Castañeda^{2,3,§}

¹*Département de Physique Théorique et Appliquée, Commissariat à l'Énergie Atomique, Bruyères-le-Châtel, F-91297 Arpajon, France.*

²*Laboratoire de Mécanique des Solides, C.N.R.S. UMR 7649,*

Département de Mécanique, École Polytechnique, 91128 Palaiseau Cedex, France

³*Department of Mechanical Engineering and Applied Mechanics,*

School of Engineering and Applied Science, University of Pennsylvania, Philadelphia, PA 19104-6315, USA

(Dated: August 26, 2021)

The overall behavior of a 2D lattice of voids embedded in an anisotropic matrix is investigated in the limit of vanishing porosity f . An effective-medium model (of the Hashin-Shtrikman type) which accounts for elastic interactions between neighboring voids, is compared to Fast Fourier Transform numerical solutions and, in the limits of infinite anisotropy, to exact results. A cross-over between regular and singular dilute regimes is found, driven by a characteristic length which depends on f and on the anisotropy strength. The singular regime, where the leading dilute correction to the elastic moduli is an $O(f^{1/2})$, is related to strain localization and to change in character — from elliptic to hyperbolic — of the governing equations.

PACS numbers: 46.05.+b,46.15.-x,46.15.Ff

I. INTRODUCTION

Effective-medium approximations (EMAs) for nonlinear composites^{1,2,3,4,5,6,7,8,9,10} (i.e., multi-phase materials), which aim to predict their overall (i.e., macroscopic) behavior, are pushed to their limits of validity as the nonlinearity and/or the heterogeneity contrast become large.⁷ Typical examples of this sort of phenomenon in continuum mechanics include porous,^{11,12,13} and rigidly reinforced,^{13,14} plastic or nonlinearly elastic media. In the idealized model of perfect plasticity, plastic material flow takes place at constant stress intensity (the yield stress). In such circumstances, the flow preferentially concentrates (*localizes*) in *shear bands*.^{15,16} Formally, these shear bands are closely related to other types of minimal breakdown manifolds in heterogeneous media (mechanical systems as well as nonlinear electrical networks).^{17,18,19} However, nonlinear EMAs which address plasticity rely on a quasi-equilibrium hypothesis, which means that the characteristic time of an individual “breakdown” (or slip) event is longer than that of wave propagation through the medium²⁰ (in nonlinear dielectrics, such conditions are met as well in the reversible diode network experiment²¹). Plastic deformation being a strongly irreversible process, applications of such EMAs to plasticity should therefore be restricted to *incipient* deformation in an incremental framework.^{12,15} Nonetheless, upon neglecting elasticity and assuming plastic incompressibility, the quasi-equilibrium hypothesis may extend to full-grown deformations, such as in the slip-line theory of perfect plasticity, but the governing equations are then hyperbolic.¹⁵

Efficient nonlinear EMAs rely on the use of an underlying linear comparison medium,^{22,23} which may consist in a “secant” (isotropic) approximation²⁴ to the nonlinear response of the composite. In the most recent approaches the comparison medium is anisotropic, of direction determined by the applied field,⁶ and of strength being consistently determined by the covariance tensors of the local fields in the phases.^{8,9,10} How these methods cope with localization at the overall level in

heterogeneous media is not well understood, see Ref. 25 and references therein.

To address this issue, this paper is devoted to the signature of incipient localization in an EMA for periodic composites.²⁶ Because for periodic media efficient methods of solution have been developed,^{25,27,28,29,30,31,32,33,34} our focus here is on such materials. Thus, a system consisting of a two-dimensional (2D) periodic lattice of voids embedded in a deformable matrix is considered. Aimed at understanding the hallmarks of localization in the underlying linear medium of nonlinear EMAs, we focus on the case of an elastically anisotropic *linear* matrix, of variable anisotropy.^{25,35}

The problem, described in Sec. II, admits an exact analytical solution in the particular case of *infinite* anisotropy where the governing equations acquire a hyperbolic character.^{25,35} As a consequence, the overall elastic moduli depend on the porosity f (the volume fraction of voids) as powers of $f^{1/2}$, in particular in the dilute limit $f \rightarrow 0$.²⁵ This result is at odds with usual effective-medium results, in which the first correction to a homogeneous medium is an $O(f)$,^{30,36} due to its proportionality to the number of inclusions.³⁷

But for *finite* anisotropy, the governing equations are elliptic, and no exact solution is available. The crossover to the regime of high anisotropy and its link to localization, of direct interest for nonlinear EMAs, and more generally for understanding the nature of the macroscopic yield transition,¹⁸ are investigated hereafter. For lack of exact solutions, comparisons are made between: (i) quasi-exact numerical results obtained by Fast Fourier Transform (FFT) calculations; (ii) outcomes of an EMA for linear periodic media whose predictive capabilities are assessed; and (iii) the exact results of Ref. 25. The case of a non-linear (visco-)plastic matrix, of direct experimental relevance,³⁸ is examined elsewhere.³⁹

The notation used is as follows: \mathbb{A} denotes a tensor of components A_{ijkl} ; the sans-serif a is the tensor of components a_{ij} (except for the strain and stress ε and σ , and the strain polarization τ , written in boldface); the boldface \mathbf{a} is the vector of components a_i . A colon denotes a double contraction e.g,

$\mathbb{A} : \mathbb{B}$ has components $A_{ijmn}B_{mnlk}$, etc. For convenience, indices $i = x, y$ or $1, 2$ are used indifferently hereafter.

II. PROBLEM FORMULATION

The composite, described in Fig. 1, consists of an elastic matrix (phase $\alpha = 1$, of volume fraction $c^{(1)} = 1 - f$), containing a square array of voided cylinders of radius a (phase $\alpha = 2$, of volume fraction $c^{(2)} \equiv f = \pi a^2$). Here and henceforth, the size of the unit cell is $L = 1$. A set of duality relations⁴⁰ allows one to translate the following results for the overall behavior of this porous medium, in the context of rigidly reinforced composites, which is another interesting case of infinite elastic contrast.

In the composite $\boldsymbol{\sigma}(\mathbf{x}) = \mathbb{L}(\mathbf{x}) : \boldsymbol{\varepsilon}(\mathbf{x})$, where $\mathbb{L}(\mathbf{x})$ is the position-dependent elasticity tensor, of components $L_{ijkl} = L_{ijlk} = L_{klij}$. The equilibrium equation $\partial_i \sigma_{ij} = 0$ holds, and the strain derives from the displacement \mathbf{u} as $\varepsilon_{ij} = (\partial_i u_j + \partial_j u_i)/2$ (small perturbations are assumed). In two dimensions, $\varepsilon_{xx} = \partial_x u_x$, $\varepsilon_{yy} = \partial_y u_y$, and $\varepsilon_{xy} = (\partial_x u_y + \partial_y u_x)/2$. In the voids, $\mathbb{L}(\mathbf{x}) = \mathbb{L}^{(2)} \equiv 0$, the stress vanishes, and the strain is arbitrary: any continuation matching the displacements at the voids boundaries is admissible. Only its volume average over the void is physically relevant.

The matrix material can be thought of as a ‘‘mixture’’ of two basic types of anisotropic media:²⁵ (i) one where the eigendirections of anisotropy coincide with the reference axes of unit vectors $\mathbf{e}_1 \equiv \mathbf{e}^x$ and $\mathbf{e}_2 \equiv \mathbf{e}^y$; and (ii) one where they coincide with the diagonals (see Fig. 1). Such a medium is invariant under the dihedral point-symmetry group D_4 .⁴¹ Then, its elastic tensor $\mathbb{L}^{(1)}$ is of the form

$$(L_{1111} + L_{1122})\mathbb{J} + 2L_{1212}\mathbb{E}^{\text{SS}} + (L_{1111} - L_{1122})\mathbb{E}^{\text{PS}}, \quad (1)$$

where \mathbb{J} , $\mathbb{E}^{\text{SS,PS}}$ are mutually orthogonal projectors defined by (\mathbb{I} , of components δ_{ij} , is the 2×2 identity matrix):

$$\mathbb{J} \equiv (1/2) \mathbb{I} \otimes \mathbb{I}, \quad (2a)$$

$$\mathbb{E}^{\text{SS,PS}} \equiv (1/2) \mathbf{e}^{\text{SS,PS}} \otimes \mathbf{e}^{\text{SS,PS}}. \quad (2b)$$

The identity is $\mathbb{I} = \mathbb{J} + \mathbb{E}^{\text{SS}} + \mathbb{E}^{\text{PS}}$. The definitions involve the so-called *simple shear* (SS) and *pure shear* (PS) eigenmodes of deformation:

$$\mathbf{e}^{\text{SS}} \equiv \mathbf{e}_1 \otimes \mathbf{e}_2 + \mathbf{e}_2 \otimes \mathbf{e}_1, \quad (3a)$$

$$\mathbf{e}^{\text{PS}} \equiv \mathbf{e}_1 \otimes \mathbf{e}_1 - \mathbf{e}_2 \otimes \mathbf{e}_2, \quad (3b)$$

such that $\mathbb{E}^{\text{SS,PS}} : \mathbf{e}^{\text{SS,PS}} = \mathbf{e}^{\text{SS,PS}}$. Their eigenvectors are related by a 45° rotation (see Fig. 1). Also, $\mathbb{J} : \mathbb{I} = \mathbb{I}$. This decomposition relates to that of a 2×2 symmetric tensor into one *equibiaxial* (i.e. compressive) mode and two orthogonal shear modes:

$$\mathbf{a} = a_m \mathbb{I} + a_{\text{SS}} \mathbf{e}^{\text{SS}} + a_{\text{PS}} \mathbf{e}^{\text{PS}}, \quad (4)$$

of respective components $a_m \equiv (a_{xx} + a_{yy})/2$, $a_{\text{SS}} \equiv a_{xy}$, $a_{\text{PS}} \equiv (a_{xx} - a_{yy})/2$. Thus, in the matrix we write:

$$\mathbb{L}(\mathbf{x}) = \mathbb{L}^{(1)} \equiv 2\kappa \mathbb{J} + 2\lambda \mathbb{E}^{\text{SS}} + 2\mu \mathbb{E}^{\text{PS}}. \quad (5)$$

κ is the bulk compressibility modulus, and λ, μ are in-plane anisotropic shear moduli. With this medium of a special orthotropic type, the interpretation of the 2D problem as a limiting one of plane stress ($\sigma_{xz} = \sigma_{yz} = \sigma_{zz} = 0, \varepsilon_{zz} \neq 0$) or of plane strain ($\varepsilon_{xz} = \varepsilon_{yz} = \varepsilon_{zz} = 0, \sigma_{zz} \neq 0$) is irrelevant from a theoretical standpoint, though the expression in terms of κ and of μ of the Young modulus and Poisson ratio relative to the pure shear mode differ in both cases.⁴²

With applications to volume-preserving plastic deformation in mind, this study mostly focuses on the limiting case of an *incompressible matrix* for which $\kappa = \infty$. Introducing in this limit the dimensionless anisotropy ratio $k = \lambda/\mu$, the medium is isotropic when $k = 1$, and is infinitely anisotropic when either $k = 0$ or $k = \infty$. In each of the latter limits, the medium possesses one infinitely hard, and one infinitely soft eigenmodes of strain: when $k = 0$ (i.e. $\lambda = 0$ or $\mu = \infty$) the medium is soft for SS loadings, and resists PS loadings, whereas when $k = \infty$ (i.e. $\lambda = \infty$ or $\mu = 0$) the medium is soft for PS loadings, and resists SS loadings. We accordingly call these loading modes ‘‘hard’’ and ‘‘soft’’ hereafter. This model provides a convenient framework for studying the coupling between porosity and localization.

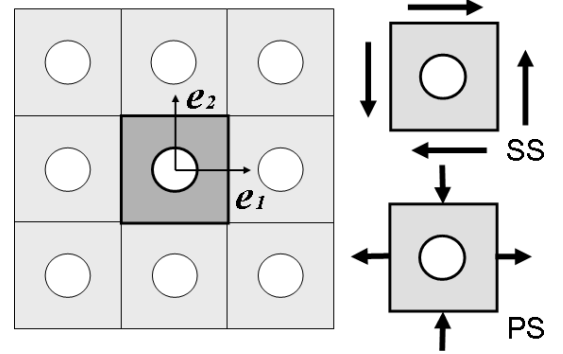


FIG. 1: Left, periodic porous medium with unit cell and reference axes. Right, black arrows depict eigenmodes of strain: simple shear (SS), and pure shear (PS).

Volume averages over the whole system are denoted by brackets $\langle \cdot \rangle$. Hereafter, $\langle \cdot \rangle^{(\alpha)}$ stands for a volume average over phase α . By definition, the effective (overall) tensor of elastic moduli, $\tilde{\mathbb{L}}$, relates the macroscopic strain $\bar{\boldsymbol{\varepsilon}} = \langle \boldsymbol{\varepsilon} \rangle$ to the macroscopic stress $\bar{\boldsymbol{\sigma}} = \langle \boldsymbol{\sigma} \rangle$:

$$\bar{\boldsymbol{\sigma}} = \tilde{\mathbb{L}} : \bar{\boldsymbol{\varepsilon}}. \quad (6)$$

The square void lattice also being invariant under D_4 , $\tilde{\mathbb{L}}$ is of a form analogous to (5), where κ, λ, μ , are replaced by the effective moduli $\tilde{\kappa}, \tilde{\lambda}, \tilde{\mu}$. The latter are the main quantities of interest. They depend on κ, λ, μ , and f . Even when $\kappa = \infty$, the effective modulus $\tilde{\kappa}$ is finite for the porous medium. Then, the normalized moduli $\tilde{\lambda}/\lambda, \tilde{\mu}/\mu$ depend only on k , and on f . Convenient normalizations for $\tilde{\kappa}$ are $\tilde{\kappa}/\mu$ when $\lambda \rightarrow \infty$, or $\tilde{\kappa}/\lambda$ when $\mu \rightarrow \infty$.

III. FULL-FIELD FFT APPROACH

A. Numerical method

Full-field numerical solutions of the problem are obtained using the Fourier transform method,⁴³ applied to linear composites. The method amounts to solving iteratively the Lippmann-Schwinger equation for the strain,⁴⁴

$$\varepsilon(\mathbf{x}) = \bar{\varepsilon} + \int d^2y \mathbb{G}(\mathbf{x} - \mathbf{y}) : \boldsymbol{\tau}(\mathbf{y}), \quad (7a)$$

$$\boldsymbol{\tau}(\mathbf{x}) \equiv [\mathbb{L}(\mathbf{x}) - \mathbb{L}^{(0)}] : \varepsilon(\mathbf{x}), \quad (7b)$$

where $\mathbb{L}^{(0)}$ is some arbitrary background elastic tensor. The position-dependent elastic tensor of the medium, $\mathbb{L}(\mathbf{x})$, is 0 ($= \mathbb{L}^{(2)}$) in the void and $\mathbb{L}^{(1)}$ in the matrix. In all the numerical calculations of the paper, the latter is assumed *nearly* incompressible with $\kappa \simeq 10^3$, and no appreciable differences were observed for $\kappa \simeq 10^2$. The tensor \mathbb{G} is the periodic Green function of the background medium, such that $\int d^2x \mathbb{G}(\mathbf{x}) = 0$. In the method, the convolution in Eq. (7a) is evaluated in Fourier space, whereas (7b) is computed in direct space. The system is finely discretized as a $L \times L$ array of pixels. The bad iterative properties of (7) are alleviated through various improvements allowing for high or even infinite contrast.^{45,46,47} These schemes are used here. Fast convergence is achieved by taking $\mathbb{L}^{(0)}$ of the type (5), with the same anisotropy ratio k as $\mathbb{L}^{(1)}$, but with considerably lower moduli, namely $\kappa^0/\kappa \simeq 5 \cdot 10^{-4}$ and $\mu^0/\mu \simeq \lambda^0/\lambda \simeq 0.2$ (not necessarily optimal values). The Fourier transform of \mathbb{G} reads⁴⁸

$$G_{ijkl}(\mathbf{q}) = - \left\{ q_i [N^{-1}(\mathbf{q})]_{jk} q_l \right\}_{\text{sym}} \quad (8)$$

where $\{\cdot\}_{\text{sym}}$ indicates a symmetrization so that $G_{ijkl} = G_{klij} = G_{jikl}$, and where $N_{ij}(\mathbf{q}) = q_k L_{iklj}^{(0)} q_l$ is the acoustic tensor.

Calculations are carried out for various anisotropy ratios $10^{-4} \leq k \leq 10^4$, and porosities $0 < f < f_c$ using FFT routines. Three sizes $L = 512, 1024, 2048$ are considered to monitor size effects. The smallest one leads to results with satisfactory convergence properties, except in cases of high anisotropy where a better resolution was required to render the fine structure of the field patterns. We used $L = 2048$ whenever an appreciable difference was found between $L = 512$ and 1024.

Once the strain $\varepsilon_{ij}(\mathbf{q})$ is computed, the displacement $\mathbf{u}(\mathbf{q})$ is deduced from $(\mathbf{q} \neq \mathbf{0})$:⁴⁹

$$\begin{aligned} u_x(\mathbf{q}) &= -i \{ q_x [\varepsilon_{xx}(\mathbf{q}) - \varepsilon_{yy}(\mathbf{q})] + 2q_y \varepsilon_{xy}(\mathbf{q}) \} / q^2, \\ u_y(\mathbf{q}) &= i \{ q_y [\varepsilon_{xx}(\mathbf{q}) - \varepsilon_{yy}(\mathbf{q})] - 2q_x \varepsilon_{xy}(\mathbf{q}) \} / q^2 \end{aligned}$$

Only SS or PS *macroscopic* strain loadings are considered ($\bar{\varepsilon}_m = 0$). Other shear states follow from linearity. For both modes, the linear elastic problem is solved for various anisotropy ratios $0 \leq k \leq \infty$. Effective moduli are computed using one component at a time, e.g. $\tilde{\lambda} = \langle \sigma_{xy} \rangle / [2 \langle \varepsilon_{xy} \rangle]$.

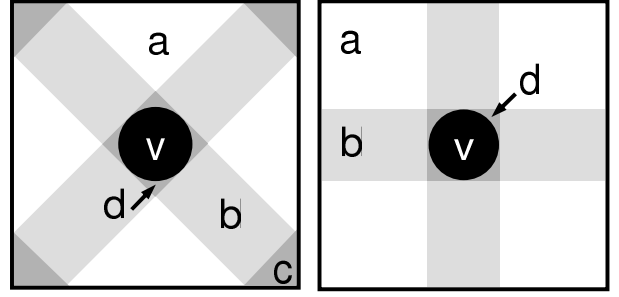


FIG. 2: Structure of unit-cell field patterns for high anisotropy. Left, pattern for SS loading and $k = \infty$. Right, pattern for PS loading and $k = 0$. In these figures, v = void; b, c, d = deformation bands in the matrix (not intersecting, intersecting far from the void, and intersecting around the void, respectively); a = remaining parts of the matrix.

B. Overview: displacement and stress maps

Typical displacement and stress maps obtained by (isochoric) FFT calculations are as follows. Since first-order infinitesimal displacements are used, it should be borne in mind that however singular, the displacement patterns are at most incipient ones. In limits of infinite anisotropy $k \rightarrow 0, \infty$, the structure of the solutions tends towards that schematized in Fig. 2, being organized into *bands* of width one void diameter. Two remarkable types of structures are found, depending on the loading direction and on the type of anisotropy. They differ essentially by the presence of zones in the matrix where the bands cross (denoted by c in Fig. 2).

With the above mentioned caveat, the following approximate symmetry holds between the maps:²⁵

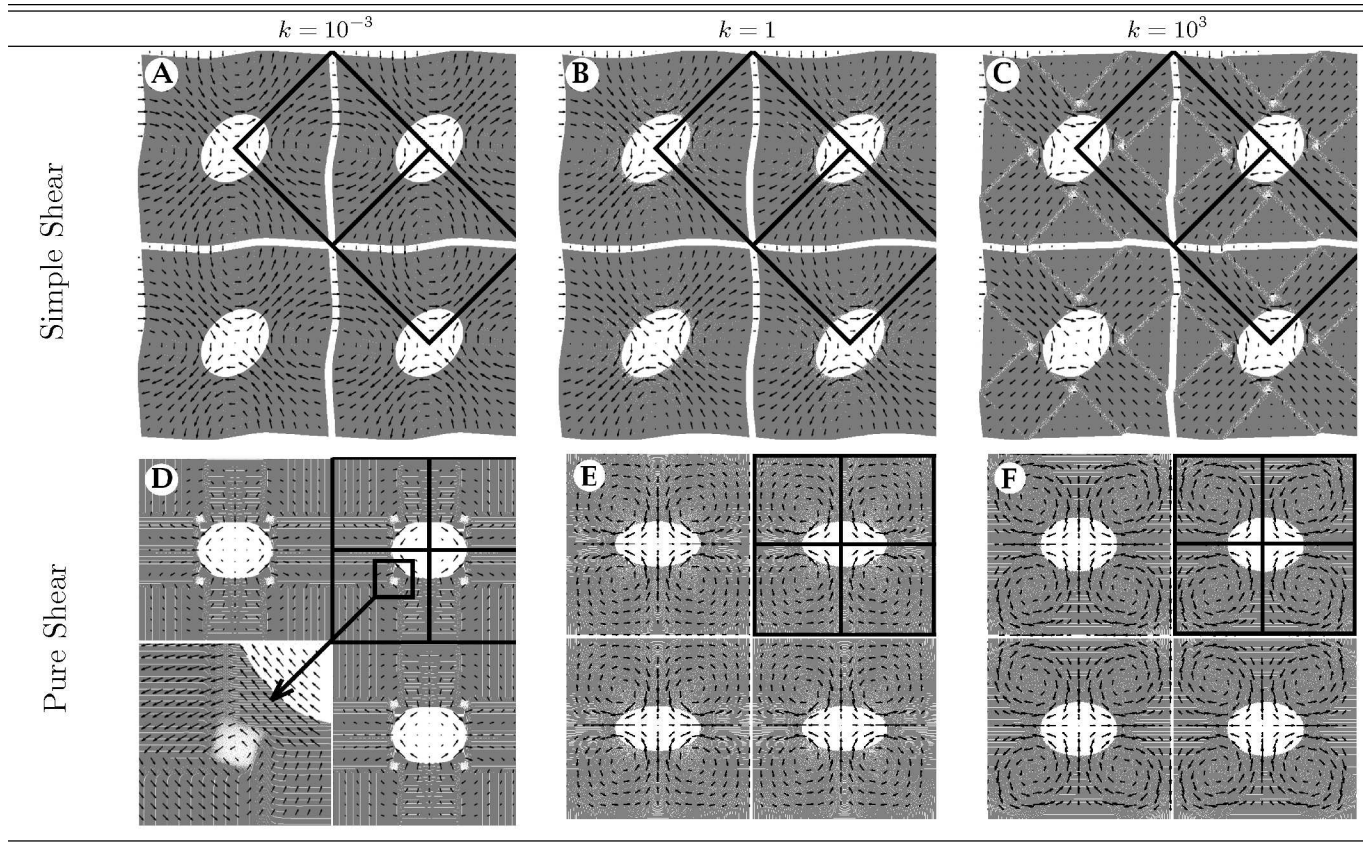
$$\mathcal{R}_{45^\circ}(\text{void lattice}) \Leftrightarrow \begin{cases} k \leftrightarrow 1/k \\ \text{PS loading} \leftrightarrow \text{SS loading}, \end{cases} \quad (9)$$

where the \mathcal{R} symbol denotes a 45° rotation of the lattice of voids, with all other parameters (material constitutive law and loading) conserved. These field structures, already revealed by the analytical calculations of Ref. 25 for infinite anisotropy (to which we refer the reader for further details), are retrieved here for finite, but high, anisotropy.

Table I displays full-field calculations of the reduced (periodic) displacement field $\mathbf{u}^*(\mathbf{x}) \equiv \mathbf{u}(\mathbf{x}) - \bar{\varepsilon} \cdot \mathbf{x}$, indicated by arrows, superimposed on a representation of the unit cell deformed using a rescaled displacement $\beta \mathbf{u}^*(\mathbf{x})$, for anisotropy ratios $k = 10^{-3}, 1, 10^3$ in SS and PS loadings, for a moderate porosity $f = 0.1$. To highlight the deformation pattern, the magnification factor β lies between 1 and 10. Lighter grey tones in the deformed matrix indicate regions subjected to a strong extension. The unit cell is replicated in order to emphasize the displacement (“flow”) pattern. For low and high k , the features of the displacement maps are in agreement with the exact results derived at infinite anisotropy in Ref. 25, which they enlighten.

The flow pattern is organized in closed convection cells of square shape, delimited by black boxes. Two types of cells, rotated 45° with respect to the Cartesian axes, and related

TABLE I: Reduced displacement field \mathbf{u}^* (arrows), and resulting elastic deformation of the unit cell (to lowest order of perturbations), in SS and PS loadings for anisotropy ratios $k = 10^{-3}$, 1 , 10^3 . An enlargement of a void is shown in map (D).



by a mirror symmetry, suffice to account for the flow pattern in SS (maps A, B, C). As a consequence, and due to the high anisotropy, the edges of the unit cells in (A) and (C) undergo non-zero and quasi piecewise-linear deformation. On the other hand, four types of convection cells, aligned along the Cartesian axes, related by mirror symmetries with respect to these axes, and fully enclosed within one unit cell, are required to produce the flow pattern in PS (D, E, F).

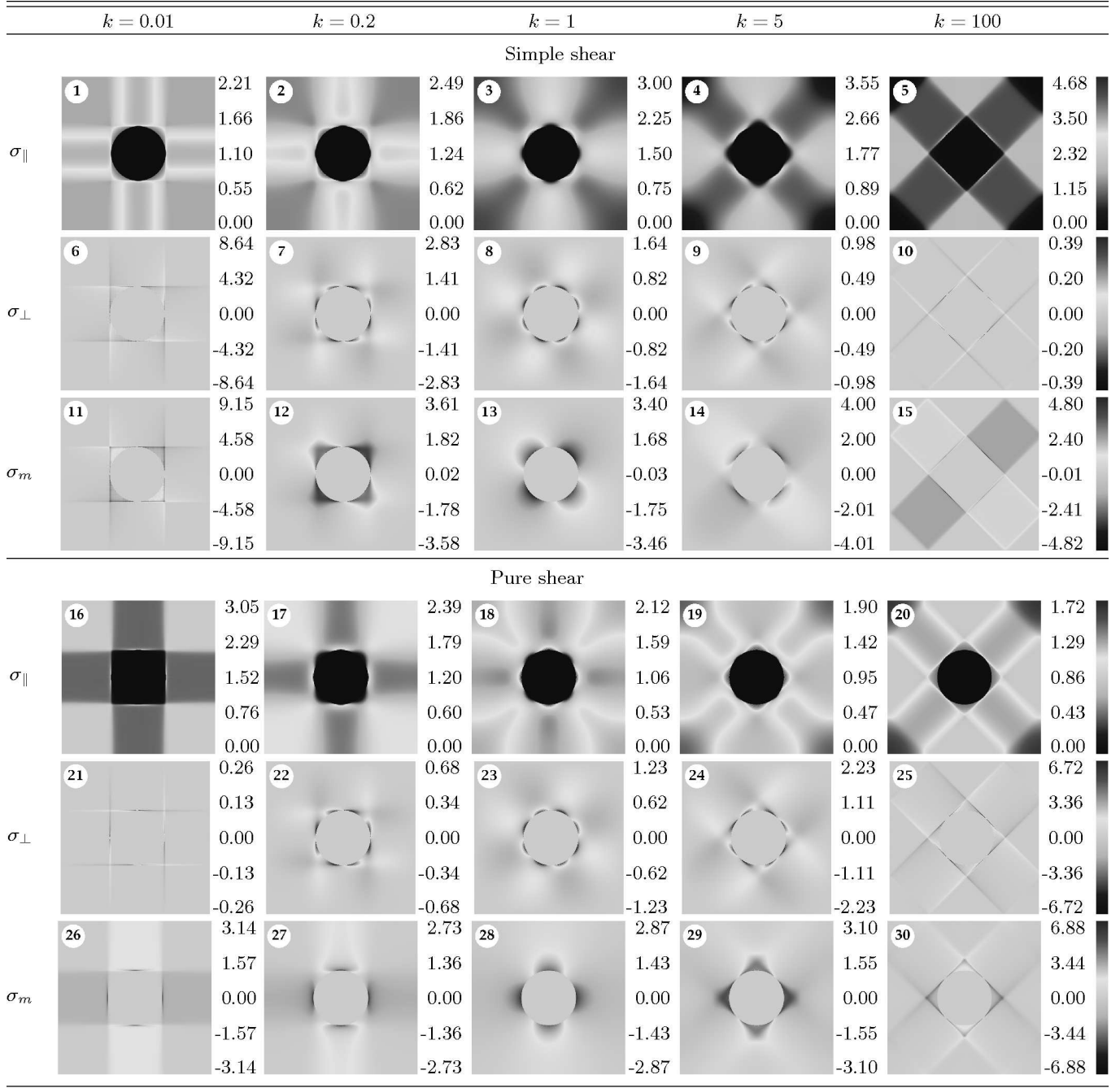
Compared to the $k = 1$ isotropic solutions of (B) and (E), solutions for highly anisotropic situations are either: (i) *localized in strain*, with a displacement field discontinuous at places [maps (C) and (D)]; (ii) *localized in stress*, with continuous displacement as in (A) and (F). Strain-localization arises whenever loading along a “hard” mode takes place. Then, the highly anisotropic medium resists most the applied strain and undergoes both a high induced stress and a weak induced strain. In the limit of infinite anisotropy, a rigid “block sliding” incipient pattern results, where the flow is organized in bands of width one void diameter (see also Fig. 2), where the tangential component of \mathbf{u}^* is discontinuous, and where strain concentrates as Dirac distributions along the sliding lines. This pattern is tantamount to a breakdown mechanism. In turn, block sliding leaves four incipient voids in the matrix in (C) and (D), at locations where the sliding lines intersect at 90° . One such void is enlarged in (D). One important difference between cases (C) and (D) is that in (C), the flow bands

(of width one void diameter) cross inside the matrix due to their 45° orientation. Flow redistribution then takes place in the intersection zones. On the contrary, in (D) such zones do not exist in the matrix, and flow redistribution requires a non-zero displacement component normal to the band boundaries. As a result, the gradient of the tangential component of \mathbf{u}^* is higher in (C) than in (D).

Solutions with a continuous displacement field are obtained instead when loading is applied along the soft deformation mode. The remaining deformation mode being harder, this leaves less possibilities for easy deformation than in the isotropic case; this explains why the unit cells of (A) and (F) are much less deformed – a magnification $\beta = 10$ is used – than the cells (B) and (E) of the isotropic material – plotted with $\beta = 1$.

Table II displays, for $f = 0.1$ and for increasing anisotropy ratios k , maps of the independent stress components σ_m , σ_{\parallel} , and σ_{\perp} , under SS and PS loadings. Hereafter, the maps are referred to by their individual number (1 to 30). Each map goes along with its own field scale at its right, in correspondence with the color scale at the extreme right of the rows. The “parallel” (\parallel) and “perpendicular” (\perp) notations refer to the “direction” of the applied macroscopic loading. The SS and PS shear components of the stress are defined in Eq. (4). In PS loading, we have $\sigma_{\parallel} \equiv \sigma^{\text{PS}}$, $\sigma_{\perp} \equiv \sigma^{\text{SS}}$, whereas in SS loading: $\sigma_{\parallel} \equiv \sigma^{\text{SS}}$, $\sigma_{\perp} \equiv \sigma^{\text{PS}}$ (hereafter, a similar notation is used

TABLE II: (Color online) Parallel (σ_{\parallel}), transverse (σ_{\perp}), and mean (σ_m) stress field maps for SS and PS loadings, with anisotropy ratios $k = 0.01, 0.2, 1, 5, 100$ (porosity $f = 0.1$). The stress fields are rescaled such that $\langle \sigma_{\parallel} \rangle = 1$



for strain components). In both cases, the volume average of the non-parallel components vanish: $\langle \sigma_{\perp} \rangle = \langle \sigma_m \rangle = 0$. The maps display rescaled stresses, such that $\langle \sigma_{\parallel} \rangle = 1$. Due to linearity, the strain fields are the same, up to a change of scale (although the scales are different in the parallel and perpendicular directions due to the anisotropy).

The following observations are relevant to the regime of high anisotropy, where the stress patterns follow that of Fig. 2. The zones where bands cross depicted in this figure [either in the matrix (zones c) or close to the voids (zones $d+v$)],

are places of additive screening or enhancement of the stress. Thus, the parallel stress in zone c of map 20 reaches its highest values there, and is twice that in the two crossing bands (however, a much higher transverse stress is encountered in the immediate vicinity of the void, see map 25). In a similar way, the vanishing stress in zone c in map 5 is the difference between the stresses in the bands. Two remarks, strictly valid for infinite anisotropy, are in order at this point: first, zones of vanishing stress are squares, of size determined by the void cross section transverse to the bands, so that the disk-like shape of

the voids is no longer relevant; second, the build-up of zones of zero stresses (i.e., analogous to porous zones) in the matrix in SS loading leads to an effective doubling of the porosity in the effective shear modulus $\tilde{\lambda}$ at infinite anisotropy, whereby an effective “close packing” threshold, twice as small as the geometric one,²⁶ is reached as f increases, leading to a “mechanically advanced” percolative behavior. As a consequence, $\tilde{\lambda}$ decays rapidly with f , see next section.

The stress is less singular than the strain in the limit of infinite anisotropy. Indeed, in a strain-localized situation (loading along a “hard” mode [maps 5, 16]), the displacement is discontinuous. Accordingly, the transverse strain has Dirac singular components along the band frontiers. They abruptly change sign at the special points $(\pm a, 0)$ and $(0, \pm a)$ on the void boundary in PS and at points $(\pm a, \pm a)/\sqrt{2}$ in SS, where a is the void radius. Because of the stress-strain proportionality, these strain singularities can be traced in maps 10 and 21. However, since the perpendicular stress vanishes in the limits $k \rightarrow 0, \infty$, so do its Dirac singularities, as shown by the small values on the scales. The special points, termed *hot spots* in Ref. 25 are points of extreme matter separation, or crushing, which bear the main cost of the “block sliding” patterns. On the other hand, the incipient secondary voids in maps (C) and (D) of Tab. I appear (somehow paradoxically) as regions of moderate stress levels.

More generally, the stress field undergoes the following types of singular behavior in the limiting cases of infinite anisotropy:

— *loading along a hard mode*: discontinuous σ_{\parallel} component along band frontiers in the direction normal to the frontiers, with finite jump, accompanied by hot spots at the void boundary [maps 5, 16];

— *loading along a soft mode*: discontinuous derivative of σ_{\parallel} in the same direction, with infinite jump [maps 1, 20], and discontinuous σ_{\perp} with infinite jump across the band frontiers (case of loading along a soft mode) [maps 6, 25].

The mean stress is always singular with the most singular behavior: it has the singularity of the parallel stress in the case of loading along a soft mode, and the singularity of the transverse stress in the case of loading along a hard mode (but the mean strain vanishes in the limit of an incompressible medium).

IV. ANALYTICAL EFFECTIVE MEDIUM APPROACH

Nemat-Nasser proposed²⁷ an approximate (dipolar) Fourier-mode approach to the periodic problem, which proved excellent for isotropic components.^{28,50} We apply it to the anisotropic case. More accurate schemes going beyond the dipolar level, however less suitable to analytical treatment, are available.^{27,29,32}

The approach is as follows. Consider first the general case of a binary composite of volume $V \rightarrow \infty$, the inclusions of which have an elastic tensor $\mathbb{L}^{(2)}$, and set $\delta\mathbb{L} = \mathbb{L}^{(2)} - \mathbb{L}^{(1)}$. The characteristic function χ_{∞} of an infinite periodic array of identical inclusions, of characteristic function χ , is $\chi_{\infty}(\mathbf{x}) = \sum_i \chi(\mathbf{x} - \mathbf{r}_i)$, where \mathbf{r}_i are lattice vectors. Then, $\mathbb{L} = \mathbb{L}^{(1)} + \chi_{\infty} \delta\mathbb{L}$. Equations (7), (8) apply, with $\mathbb{L}^{(0)} = \mathbb{L}^{(1)}$, and $\boldsymbol{\tau} =$

$\chi_{\infty} \delta\mathbb{L} : \boldsymbol{\varepsilon}$. Multiplying (7a) by χ , integrating over V , and assuming homogeneous deformation in the inclusions so that $\chi_{\infty} \boldsymbol{\varepsilon} = \chi_{\infty} \langle \boldsymbol{\varepsilon} \rangle^{(2)}$,⁵¹ results in an expression of $\langle \boldsymbol{\varepsilon} \rangle^{(2)}$ in terms of the Hill depolarization tensor^{52,53} of the lattice

$$\begin{aligned} \mathbb{P} &= -\frac{1}{Vc^{(2)}} \int d^2x d^2x' \chi_{\infty}(\mathbf{x}) \mathbb{G}(\mathbf{x} - \mathbf{x}') \chi_{\infty}(\mathbf{x}') \\ &= -V_I \int \frac{d^2\mathbf{q}}{(2\pi)^2} \sum_{\mathbf{r}} e^{i\mathbf{q}\cdot\mathbf{r}} \mathbb{G}(\mathbf{q}) |\langle e^{i\mathbf{x}\cdot\mathbf{q}} \rangle_I|^2 \end{aligned} \quad (10)$$

$$= -c^{(2)} \sum'_{\substack{\mathbf{q}=2\pi\mathbf{p} \\ \mathbf{p}\in\text{R.L.}}} \mathbb{G}(\mathbf{q}) |\langle e^{i\mathbf{x}\cdot\mathbf{q}} \rangle_I|^2, \quad (11)$$

where $\langle \cdot \rangle_I$ denotes a volume average over *one* individual inclusion of volume V_I . The sum in (10) is over lattice sites. The last equality stems from the Poisson summation formula.⁵⁴ The primed sum is over nonzero reciprocal lattice vectors $\mathbf{p} = (p_x, p_y)$ (with integer components). Carrying over the obtained $\langle \boldsymbol{\varepsilon} \rangle^{(2)}$ to the volume average $\langle \mathbb{L} : \boldsymbol{\varepsilon} \rangle$ computed from (7), and using definition (6), entails the effective elastic tensor

$$\tilde{\mathbb{L}} = \mathbb{L}^{(1)} + c^{(2)} \delta\mathbb{L} : (\mathbb{I} + \mathbb{P} : \delta\mathbb{L})^{-1}. \quad (12)$$

The formula for the void lattice with $\mathbb{L}^{(2)} = 0$ follows.

Equ. (12) is of the Hashin-Shtrikman (HS) variational type.^{55,56,57} In particular, the void lattice version provides an upper bound to the exact result.⁵⁰ Interpreted in the framework of multiple-scattering theory,^{58,59} Equ. (12) states that, at the dipolar level, the effect of the inclusion lattice on the homogeneous matrix amounts to that of *non-interacting* identical “equivalent” inclusions in proportion $c^{(2)}$, characterized by a T -matrix provided by the term following $c^{(2)}$ in (12);^{58,59} furthermore, each of these equivalent inclusions possesses a lattice, $c^{(2)}$ -dependent, microstructure, the influence of which is lumped in \mathbb{P} . To make contact with other types of effective-medium expressions, separate \mathbb{P} into one and two-body contributions⁵⁸ by writing $\mathbb{P} \equiv \mathbb{P}_1 - c^{(2)} \mathbb{P}_2$, where \mathbb{P}_1 is the $\mathbf{r} = \mathbf{0}$ term in (10). A similar decomposition is proposed in Ref. 60 in the context of random composites. Then, introducing $\delta\tilde{\mathbb{L}} = \tilde{\mathbb{L}} - \mathbb{L}^{(1)}$, (12) takes on the familiar HS form with pair correlations⁴⁸ $\tilde{\mathbb{T}} = c^{(2)} \mathbb{T}_1$ where,

$$\tilde{\mathbb{T}} \equiv \delta\tilde{\mathbb{L}} : \left(\mathbb{I} + \mathbb{P}_2 : \delta\tilde{\mathbb{L}} \right)^{-1}, \quad \mathbb{T}_1 \equiv \delta\mathbb{L} : \left(\mathbb{I} + \mathbb{P}_1 : \delta\mathbb{L} \right)^{-1}. \quad (13)$$

This decomposition proves useful whenever some eigenvalue of \mathbb{T}_1 should blow up. Then, the corresponding eigenvalue of $\delta\tilde{\mathbb{L}}$ is simply provided by that of $-\mathbb{P}_2^{-1}$, as the above expression makes clear.

For cylindrical voids of radius a , with J_1 the Bessel function, $\langle e^{i\mathbf{q}\cdot\mathbf{x}} \rangle_I = 2J_1(aq)/(aq)$. Setting

$$m \equiv \mu/\kappa, \quad \ell \equiv \lambda/\kappa, \quad (14)$$

one finds from (8), (11) that $P_{ijkl} = \{Q_{ipql}R_{jpqk}\}_{\text{sym}}$, where $\mathbb{R} = \mathbb{J} - (1+m)\mathbb{E}^{\text{SS}} - (1+\ell)\mathbb{E}^{\text{PS}}$, where “sym” denotes a symmetrization with respect to indices (i, j) and (k, l) , and

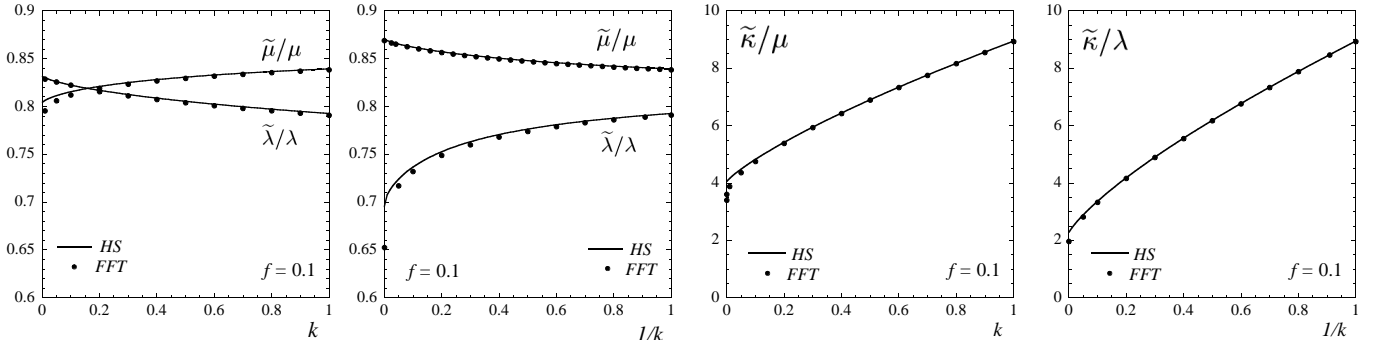


FIG. 3: Effective shear ($\tilde{\lambda}$, $\tilde{\mu}$) and compressibility ($\tilde{\kappa}$) moduli vs. anisotropy ratio k . Incompressible matrix. Comparisons between the EMA (solid lines) and FFT results (dots) for porosity $f = 0.1$. The quantity $\tilde{\kappa}$ is normalized with respect to the most appropriate modulus, depending on the range of k considered.

where

$$\mathbb{Q} = \frac{2}{\pi} \sum'_{\mathbf{p} \in \text{R.L.}} \frac{J_1^2(2\pi ap)}{p^2 \Delta(\mathbf{p})} \mathbf{p} \otimes \mathbf{p} \otimes \mathbf{p} \otimes \mathbf{p}, \quad (15a)$$

$$\Delta(\mathbf{p}) = \lambda(1+m)(p_x^2 - p_y^2)^2 + 4\mu(1+\ell)p_x^2 p_y^2. \quad (15b)$$

The reciprocal lattice is a square lattice. Hence \mathbb{Q} is also invariant under D_4 . Being completely symmetric, it is of type (1) with $L_{1122} = L_{1212}$ and is determined by two independent scalar lattice sums only. One obtains:

$$\mathbb{Q} = \frac{1}{\mu(1+\ell)} [(S_\lambda + S_\mu)\mathbb{J} + S_\mu \mathbb{E}^{\text{SS}} + S_\lambda \mathbb{E}^{\text{PS}}], \quad (16)$$

where, after having reduced the lattice sums to sums over the positive quadrant,

$$\left. \begin{array}{l} S_\lambda \\ S_\mu \end{array} \right\} = \frac{4}{\pi} \sum_{\substack{p_x \geq 0 \\ p_y \geq 1}} \frac{J_1^2(2\pi ap)}{p^2 [4p_x^2 p_y^2 + k(p_x^2 - p_y^2)^2]} \left\{ \begin{array}{l} (p_x^2 - p_y^2)^2 \\ 4p_x^2 p_y^2 \end{array} \right. \quad (17)$$

These sums bring in the anisotropy parameter:

$$k \equiv [(1+m)\lambda]/[(1+\ell)\mu] \quad (18)$$

which reduces to λ/μ in the incompressible limit $\kappa \rightarrow \infty$. We remark in passing that

$$kS_\lambda + S_\mu = S_2(a) \equiv \frac{4}{\pi} \sum_{\substack{p_x \geq 0, p_y \geq 1}} [J_1(2\pi ap)/p]^2 \quad (19)$$

is independent of k . After some algebra, one arrives at

$$\mathbb{P} = \frac{1}{2\mu(1+\ell)} \{ (\ell S_\lambda + m S_\mu)\mathbb{J} + [m S_\mu + (1+m)S_\lambda]\mathbb{E}^{\text{SS}} + [\ell S_\lambda + (1+\ell)S_\mu]\mathbb{E}^{\text{PS}} \}. \quad (20)$$

The one-body \mathbb{P}_1 is read from this expression, provided that $S_{\lambda,\mu}$ are computed in the continuum limit, by making the substitutions $\sum \rightarrow \frac{1}{4} \lim_{\epsilon \rightarrow 0} \int_{\epsilon}^{\infty} d^2q/(2\pi)^2$, $\mathbf{p} \rightarrow \mathbf{q}/(2\pi)$ in (17). Then (in the continuum limit), $S_{\lambda,\mu} \rightarrow$

$$S_{1\mu} \equiv \frac{1}{1 + \sqrt{k}}, \quad S_{1\lambda} \equiv \frac{1}{(1 + \sqrt{k})\sqrt{k}}. \quad (21)$$

Eqs. (17) show that S_λ blows up when $k \rightarrow 0$ due to the contribution of the Cartesian axis $p_x = 0$. On the other hand, S_μ remains finite or goes to zero in all cases.

The limit of an isotropic matrix where $k = 1$, $\ell = m = \kappa/\mu$ provides $\mathbb{P}_1 = [2m\mathbb{J} + (1+2m)\mathbb{K}]/[4\mu(1+m)]$, where $\mathbb{K} \equiv \mathbb{E}^{\text{SS}} + \mathbb{E}^{\text{PS}}$. This expression can be recovered directly from (8) and from the usual definition in terms of an angular integral⁶¹ $\mathbb{P}_1 = -\int d^2\Omega_{\hat{\mathbf{q}}} \mathbb{G}(\hat{\mathbf{q}})/(2\pi)$ where $\hat{\mathbf{q}} = \mathbf{q}/q$ (the independence wrt. χ stems from the rotational symmetry of the voids).

From (12), (20), the effective moduli of the void lattice read, with $f = c^{(2)}$:

$$\tilde{\kappa}/\mu = 1 - f / \{1 - [(\lambda/\mu)S_\lambda + S_\mu]/(1+\ell)\}, \quad (22a)$$

$$\tilde{\lambda}/\lambda = 1 - f / \{1 - k[S_\lambda + mS_\mu]/(1+m)\}, \quad (22b)$$

$$\tilde{\mu}/\mu = 1 - f / \{1 - [S_\mu + mS_\lambda]/(1+\ell)\}. \quad (22c)$$

Henceforth, incompressibility is assumed for simplicity so that $k \equiv \lambda/\mu$ from now on, unless explicitly stated.

V. RESULTS

A. Effective moduli

The numerical results at various values of k and f discussed in this section are obtained using brute force numerical computations of the sums $S_{\lambda,\mu}$, with convergence checks. The sums $S_{\lambda,\mu}$ are conditionally (and slowly) convergent and the following suitable prescription is used. Sums are carried out over concentric square shells of points $S_n = \{(p_x, n) | 0 \leq p_x \leq n-1\} \cup \{(n, p_y) | 1 \leq p_y \leq n\}$ for $1 \leq n \leq N$, with N is sufficiently large. Huge numbers of terms are required for accuracy, especially in the dilute limit.

Figs. 3 show comparisons between the effective moduli computed numerically from the above maps, and the EMA of Sec. IV (indicated as HS in the plots), for $f = 0.1$. The agreement is excellent near the case of an isotropic matrix $k = 1$ (as is expected for such a small porosity), but also up to high anisotropy. In all cases, the EMA is seen to provide an upper

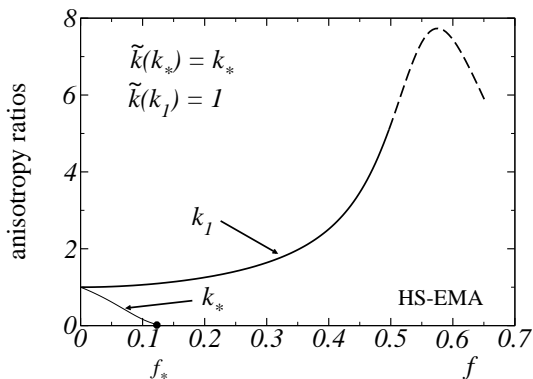


FIG. 4: Anisotropy ratios k_1 and k_* vs. porosity f in the HS-EMA. Incompressible matrix.

bound for the corresponding full-field estimates (a property of the Hashin-Shtrikman approach).

Near $k = 1$, the orientation of the void lattice makes the medium harder under PS loading, than under SS loading [i.e., $\tilde{\mu}(k = 1) > \tilde{\lambda}(k = 1)$]. Indeed, the anisotropic matrix can be thought of as containing rigidifying fibers (of strength μ), oriented at 45° along the diagonals, that resist PS deformation, and fibers (of strength λ) oriented along the Cartesian axes, that resist SS deformation. In the void lattice, the nearest neighboring voids, and consequently the largest “directional damage”, lie along the Cartesian axes, which explains the difference. We emphasize that while this observation remains true as $k \rightarrow 0$, the situation changes as $k \rightarrow \infty$: in this limit, due to the presence of the fictitious voids produced by band crossing, mentioned in the previous section, the nearest-neighboring “voids” become located along the diagonals, so that the PS direction becomes, for k higher than some value $k = k_1$ (discussed below), the most damaged one, hence the softest.

As $k \rightarrow 0$ (Fig. 3a), the curvature of the plots indicates that $\tilde{\mu}$ increases slower than μ , whereas $\tilde{\lambda}$ decreases slower than λ . As $k \rightarrow \infty$ (Fig. 3b), the parts played by λ and μ are reversed. Moreover, the compressibility modulus $\tilde{\kappa}$ decreases as anisotropy increases, in a way comparable to the hardest shear modulus (Figs. 3c and d).

At high anisotropy k , $1/k \lesssim 0.1$, discrepancies between full-field calculations and the EMA arise for the hardest shear modulus (i.e., $\tilde{\mu}$ when $k \rightarrow 0$, and $\tilde{\lambda}$ when $k \rightarrow \infty$), whereas the softest one remains extremely well reproduced. This may indicate that the lattice sums have problems dealing accurately with the effect of second-nearest-neighboring voids. Indeed, the softest direction is always the one where the voids (real, or fictitious) are nearest-neighbors, whereas the hardest one corresponds to second-nearest-neighbors. Note that $\tilde{\kappa}$, which behaves as the hardest effective modulus, suffers similar discrepancies at high anisotropy.

To discuss the crossing of the curves that takes place in Fig. 3a, consider the effective anisotropy ratio $\tilde{k} \equiv \tilde{\lambda}/\tilde{\mu}$. Crossing occurs when $\tilde{k}(k_*) = k_*$, for some $k = k_*(f)$ where the overall medium and the matrix have the same anisotropy

ratio. The point k_* , as estimated by the EMA, is represented vs. f in Fig. 4 (no attempt has been made to use full-field calculations for computational cost reasons). The $k_*(f)$ curve shows that crossing only occurs for porosities $f < f_* \simeq 0.13$: as f increases, the curve $\tilde{\lambda}/\lambda$ in Fig. 3(a) goes down to zero faster than $\tilde{\mu}/\mu$, while the crossing point shifts to the left until it vanishes. Remark that $k_* < 1$ whenever it exists. For $k < k_* < 1$, the matrix is more anisotropic than the composite; the inverse situation prevails for $k > k_*$, and in particular for $f > f_*$ where $k_* \equiv 0$, so that void-induced anisotropy dominates in this regime.

The other remarkable anisotropy ratio is the aforementioned k_1 , defined by the equation $k(k_1) = 1$, where the overall behavior is isotropic in the plane. This point, also represented on Fig. 4, exists at least up to high porosity values. However, since the EMA is expected to fail around $f = 0.5$ (see below), the irrelevant part of the $k_1(f)$ curve is sketched with dashed lines in Fig. 4. In the relevant porosity range, the fact that $k_1(f) > 1$ indicates that the matrix needs to be made harder along the SS (λ) mode than along the PS (μ) mode in order to reach isotropy, so as to compensate for higher softening in this direction due to newly appearing nearest neighboring voids, as is explained above.

Fig. 5 illustrates the behavior of the moduli with the porosity f , for finite anisotropy ratios $k = 0.01, 1, 100$, together with the exact results of Ref. 25 at $k = 0, \infty$. The exact curve for $\tilde{\mu}$ at $k = \infty$, almost superimposed with the EMA curve for $k = 100$ in (b), is available up to $f = \pi/8$ only.²⁵ Firstly, the EMA is again seen to systematically overestimate the moduli. Next, all the elastic moduli must vanish at least at the geometrical close-packing threshold of the voids,²⁶ $f = f_c = \pi/4 \simeq 0.78$, and possibly before.²⁵ The FFT points in Figs. 5a and 5b are consistent with this fact, whereas the EMA fails by producing non-zero results at this point. This is not surprising, since EMAs of the HS type are known not to be able to account for percolative-type behavior.²⁶ Moreover, the exact result in Fig. 5a for $k = \infty$ shows the shear modulus in the hard direction, $\tilde{\lambda}$, to vanish at $f = f_c/2$ due to the fictitious voids produced by band crossing. Accordingly, for large but finite k , $\tilde{\lambda}$ decreases rapidly with f up to $f = f_c/2$, then with a lower slope up to $f = f_c$. The EMA again fails to account for the threshold at $f_c/2$, although the local minimum of $\tilde{\lambda}$ at $f \simeq 0.55$ in Fig. 5a may indicate that at least part of the phenomenon is captured by the dipolar lattice sums. Interestingly enough, when available, the exact results for infinite anisotropy at $k = 0$ (resp. $k = \infty$) are seen to provide tight lower (resp. upper) bounds to the effective moduli for all values of k , and in particular to the isotropic case $k = 1$. As far as the effective moduli are concerned, Fig. 5 clearly shows that the EMA can be trusted quantitatively up to $f = 0.30$ at most, and is qualitatively reasonable (as long as the matrix is not too anisotropic) up to $f = 0.5$.

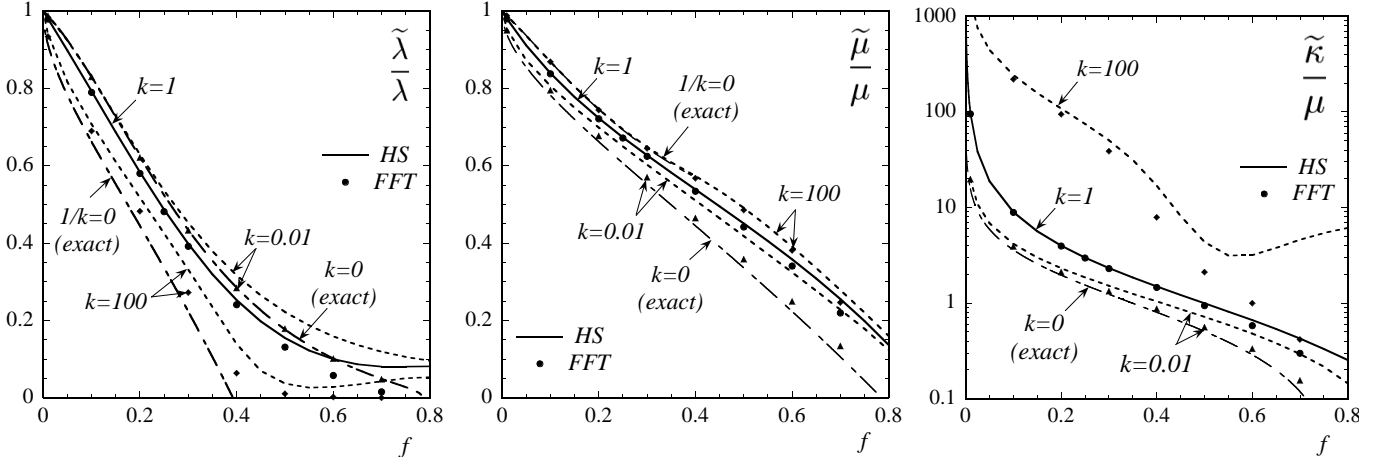


FIG. 5: Effective shear ($\tilde{\lambda}$, $\tilde{\mu}$) and compressibility ($\tilde{\kappa}$) moduli vs. porosity f for various anisotropy ratio k . Incompressible matrix. Comparisons between the EMA for $k = 1$ (solid), and $k = 0.01, 100$ (dotted); FFT results for $k = 0.01$ (triangle dots), $k = 0.01$ (circle dots), and $k = 100$ (losange dots); and exact results at $k = 0, \infty$ taken from Ref. 25 (dash-dotted).

B. Continuous transition in the dilute limit $f \ll 1$

1. Finite anisotropy

For a finite anisotropy ratio k , the dilute expressions for the effective *shear* moduli at sufficiently small f are read from expressions (22b), (22c) with $S_{\lambda,\mu}$ replaced by the one-body contributions $S_{1\lambda}$ and $S_{1\mu}$ defined in (21). For the incompressible medium, the HS estimates of the shear moduli are:

$$\tilde{\lambda}/\lambda = 1 - f(1 + \sqrt{k}) + O(f^2), \quad (23a)$$

$$\tilde{\mu}/\mu = 1 - f(1 + 1/\sqrt{k}) + O(f^2). \quad (23b)$$

As to the effective compressibility modulus, the incompressible limit leads to the situation described below Equ. (13), where one eigenvalue of \mathbb{T}_1 blows up. This requires us to go beyond the one-body approximation. However, Equ. (A.8b) in the Appendix shows that $S_2(a)$ in (19) is *exactly* $S_2 = 1 - f$ for $f < \pi/4$. Replacing, e.g. S_μ by $S_{1\mu} + O(f)$ and computing S_λ via (19), then letting $\kappa \rightarrow \infty$ in (22a) [with k read from (18)] provides:

$$\tilde{\kappa} = \sqrt{\lambda\mu}/f + O(1). \quad (23c)$$

Remark that “extended” dilute approximations, which extrapolate the above formulas for moderate anisotropy to finite (but small) porosities, result from taking $\mathbb{P}_2 = \mathbb{P}_1$ in (13), i.e. from using in (22):

$$S_{\mu,\lambda} = S_{\mu,\lambda}^{\text{dil}} \equiv (1 - f)S_{1\mu,\lambda}. \quad (24)$$

This amounts to assuming pair correlations between the voids dictated by the void shape,⁶⁰ and provides HS formulas of the “classical” type in which the lattice structure is ignored.

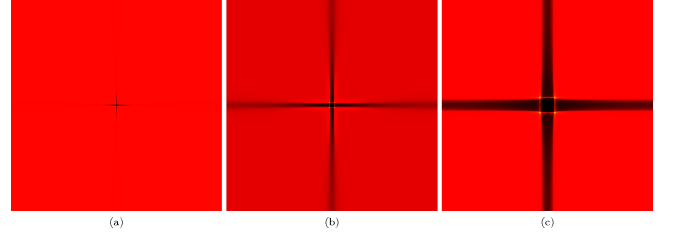


FIG. 6: (Color online) FFT computations of $\varepsilon_{\text{PS}} = \varepsilon_{\parallel}$ in PS loading, for a material with strong anisotropy ratio $k = 10^{-3} \ll 1$. Porosities from left to right: $f = f_r/10$ (regular “dilute” regime); $f = f_r$ (crossover regime); $f = 10f_r$ (“strongly anisotropic” regime), where $f_r \simeq k/\pi$ is the cross-over porosity. Incompressible matrix. Black represents the highest field values (arbitrary color scale).

2. Infinite anisotropy

After the incompressible limit $\kappa \rightarrow \infty$ is taken, the limit of infinite anisotropy $k \rightarrow 0$ is obtained by letting $\mu \rightarrow \infty$ in $\tilde{\lambda}$, and $\lambda \rightarrow 0$ in $\tilde{\mu}$. Conversely, $k \rightarrow \infty$ requires $\mu \rightarrow 0$ in $\tilde{\lambda}$, and $\lambda \rightarrow \infty$ in $\tilde{\mu}$. In these limits, the sums S_λ , S_μ in (17) are computed in the Appendix. The obtained shear moduli $\tilde{\lambda}$, $\tilde{\mu}$ are compared to the exact results of Ref. 25. One finds for $k \rightarrow 0$:

$$\frac{\tilde{\lambda}}{\lambda} = 1 - f - \frac{32}{3} \left(\frac{f}{\pi}\right)^{3/2} + 2 \left(1 - \frac{512}{9\pi^3}\right) f^2 + O(f^{5/2}), \quad (25a)$$

$$\frac{\tilde{\mu}}{\mu} = 1 - \frac{3\pi^2}{32} \left(\frac{f}{\pi}\right)^{1/2} - \frac{9\pi^3}{1024} f + O(f^{3/2}), \quad (25b)$$

$$\frac{\tilde{\kappa}}{\mu} = \frac{32}{3\pi^2} \left(\frac{\pi}{f}\right)^{1/2} - 2. \quad (25c)$$

while exact expressions are:

$$\frac{\tilde{\lambda}}{\lambda} = 1 - f - \frac{32}{3} \left(\frac{f}{\pi}\right)^{3/2} + \left(1 - \frac{6}{\pi} - \frac{8}{\pi^2}\right) f^2 + O(f^{5/2}), \quad (25d)$$

$$\frac{\tilde{\mu}}{\mu} = 1 - \left(\frac{f}{\pi}\right)^{1/2}. \quad (25e)$$

For $k \rightarrow \infty$, the HS estimates read:

$$\frac{\tilde{\lambda}}{\lambda} = 1 - \frac{3\pi^2}{16\sqrt{2}} \left(\frac{f}{\pi}\right)^{1/2} - \frac{9\pi^3}{512} \left(\frac{f}{\pi}\right) + O(f^{3/2}), \quad (26a)$$

$$\frac{\tilde{\mu}}{\mu} = 1 - f - \frac{16\sqrt{2}}{3} \left(\frac{f}{\pi}\right)^{3/2} + 2 \left(1 - \frac{256}{9\pi^3}\right) \left(\frac{f}{\pi}\right)^2 + O(f^{5/2}), \quad (26b)$$

$$\frac{\tilde{\kappa}}{\lambda} = \frac{16\sqrt{2}}{3\pi^2} \left(\frac{\pi}{f}\right)^{1/2} - 2. \quad (26c)$$

whereas exact expressions are:

$$\frac{\tilde{\lambda}}{\lambda} = 1 - \left(\frac{2f}{\pi}\right)^{1/2}, \quad (26d)$$

$$\frac{\tilde{\mu}}{\mu} = 1 - f - \frac{32}{3\sqrt{2}} \left(\frac{f}{\pi}\right)^{3/2} + \left(1 - \frac{3}{\pi} - \frac{4}{\pi^2}\right) f^2. \quad (26e)$$

The above comparisons show that the HS estimates do an excellent job of capturing the presence of half-integers powers of f in limits of infinite anisotropy at lowest orders in the dilute limit. Moreover, even when the numerical coefficients are not exact, they are close to the exact values. The less singular character of $\tilde{\lambda}$ in (25a), (25d) when $k \rightarrow 0$ [resp. $\tilde{\mu}$ in (26b), (26e) when $k \rightarrow \infty$] is discussed in Ref. 25.

3. The dilute transition

Obviously, a cross-over takes place between sets (23) on the one hand, and (25), (26) on the other hand. Balancing the ‘‘extended dilute’’ sum S_μ^{dil} (24) with $S_\mu^{k \rightarrow 0}$ [equ. (A.9b)], then with $S_\mu^{k \rightarrow \infty}$ [equ. (A.9d)] and solving for k , provides a discontinuous cross-over porosity $f_r(k)$ curve which defines in the (f, k) plane boundary lines between dilute and high-anisotropy regions. Owing to the approximations at play, this boundary cannot be trusted for k of order one (for this reason we do not display the curves). On the other hand, we find $f_r(k) \simeq (9\pi^3/1024)k \simeq k/\pi$ for $k \ll 1$ and $f_r(k) \simeq (9\pi^3/512)k^{-1} \simeq 2/(k\pi)$ for $k \gg 1$.

Due to the relation $f = \pi a^2$, the cross-over porosity in the highly anisotropic regime stems from a length scale $\xi(k)$ such that $\xi \sim a/k^{1/2}$ for $k \ll 1$, and $\xi \sim ak^{1/2}$ for $k \gg 1$. From a mathematical standpoint, these length scales originate from a scaling property of the lattice sums. We focus here on the case $k \rightarrow 0$. The case $k \rightarrow \infty$ can be discussed by adapting this argument. Introducing $K = k/(1 - k)$, the sum S_μ in (17)

can be written with a summand proportional to $[1 + K\gamma(\hat{\mathbf{p}})]^{-1}$, where the dimensionless quantity $\gamma(\hat{\mathbf{p}})$ reads

$$\gamma(\hat{\mathbf{p}}) = \frac{(p_x^2 + p_y^2)^2}{4p_x^2 p_y^2}. \quad (27)$$

Singling out the contribution of the main diagonal to S_μ , the remainder of this sum can be brought down to a sum over $p_x \geq 2$ and $1 \leq p_y \leq p_x - 1$, in which $1/4 \leq \gamma(\hat{\mathbf{p}}) \leq (p_x/1)^2$. Hence, $\gamma(\hat{\mathbf{p}}) \sim p^2$ so that $K\gamma(\hat{\mathbf{p}})$ provides an appreciable k -dependent contribution only for $p \gtrsim 1/\sqrt{K} \sim 1/\sqrt{k}$. Moreover, $[2J_1(x)/x]^2$ is appreciable only when $x \lesssim 2$. In terms of p , this reads $p \lesssim 1/(\pi a)$, see (17). Hence k -dependent terms contribute only provided that $1/\sqrt{k} \leq p \leq 1/(\pi a)$. In turn, this is possible only if $\xi(k) \lesssim 1$. For $\xi(k) \gtrsim 1$, a k -independent regime instead takes place in S_μ .

From a physical standpoint, the length scale ξ represents an *effective inclusion size*. Fig. 6 indeed displays three maps of the parallel strain field in PS loading, computed by FFT at fixed anisotropy ratio $k = 10^{-3}$ with varying porosity $f \simeq f_r/10$, f_r and $10f_r$. It is seen that localized shear bands develop from the void as porosity increases. At regime change, they coalesce and span the entire medium. The void can be considered as an isolated inclusion only for $f < f_r$. A similar effect takes place for high k values. We checked numerically that in both cases, before coalescence, the strain intensity in the bands decays exponentially as $\varepsilon \propto \exp(-br/\xi)$, where r is the distance from the void, and where b is a numerical coefficient of order one.

C. Average fields and standard deviations

1. General considerations

The first two moments of the fields are required for applications to non-linear EMAs, and can be consistently computed from any linear homogenization estimate.⁷ Hereafter, $\bar{\varepsilon}_\varepsilon^{(\alpha)} \equiv \langle \varepsilon \rangle^{(\alpha)} / \bar{\varepsilon}$ denotes the phase average of a strain component ε , normalized by the applied macroscopic field. Likewise, we denote by $SD^{(\alpha)}(\varepsilon)$ its standard deviation (SD) in phase α , *normalized by $\bar{\varepsilon}$* . Similar notations apply to stress components.

The phase-averaged fields in the porous composite are deduced from the set of equations

$$\tilde{\mathbb{L}} : \bar{\varepsilon} = (1 - f)\mathbb{L}^{(1)} : \langle \varepsilon \rangle^{(1)}, \quad (28a)$$

$$\bar{\varepsilon} = (1 - f)\langle \varepsilon \rangle^{(1)} + f\langle \varepsilon \rangle^{(2)}. \quad (28b)$$

Moreover, assuming single mode-loading, the second moments in each phase are obtained by taking a derivative of the strain energy with respect to the elastic moduli of the phases, as⁷

$$\langle \varepsilon_{\text{m,SS,PS}}^2 \rangle^{(\alpha)} = \frac{1}{c^{(\alpha)}} \frac{\partial \tilde{L}}{\partial L^{(\alpha)}} \langle \varepsilon_{\text{m,SS,PS}} \rangle^{(\alpha)}, \quad (29)$$

where \tilde{L} is $\tilde{\kappa}$ (resp. $\tilde{\lambda}, \tilde{\mu}$) when the index in the l.h.s. is m (resp. SS, PS) and where $L^{(\alpha)}$ is $\kappa^{(\alpha)}$ (resp. $\lambda^{(\alpha)}, \mu^{(\alpha)}$) when the index the r.h.s. is m (resp. SS, PS). The variances follow. If need be, the incompressibility limit is taken after these quantities are computed.

Table III displays for $f = 0.1$ the normalized phase-average strains $\bar{\varepsilon}_e^{(\alpha)}$ for $\alpha = 1, 2$ and SDs of the strain and stress components in the matrix, as computed by the EMA and by full-field calculations. The overall agreement is again excellent, the most important observed deviations, if any, occurring at small k . The table layout emphasizes the qualitative correspondence between case (k, SS) and case $(1/k, PS)$, explained in Ref. 25.

Some trends in the data are explained by appealing to the variational expression of the elastic energy W :

$$W(\bar{\varepsilon}; k; f) = \inf_{\varepsilon \in \mathcal{K}(\bar{\varepsilon})} \left\{ \frac{1}{2} \int \varepsilon : \mathbb{L} : \varepsilon \right\} = \frac{1}{2} \bar{\varepsilon} : \tilde{\mathbb{L}} : \bar{\varepsilon} \quad (30)$$

where $\mathcal{K}(\bar{\varepsilon}) = \{\varepsilon; \varepsilon_{ij} = (\partial_i u_j + \partial_j u_i)/2, \langle \varepsilon \rangle = \bar{\varepsilon}\}$ is the set of admissible strain fields. E.g., for an incompressible material under SS loading (28a) and (30) imply:

$$\bar{\varepsilon} \langle \varepsilon_{\parallel} \rangle^{(1)} = \langle \varepsilon_{\parallel}^2 \rangle^{(1)} + (1/k) \langle \varepsilon_{\perp}^2 \rangle^{(1)}. \quad (31)$$

Hence the standard deviation $SD^{(1)}(\varepsilon_{\parallel})$ of the parallel component of the strain is essentially finite, since $\langle \varepsilon_{\parallel} \rangle^{(1)}$ is, in agreement with the analytical expressions of the SDs in the next section to which we refer the reader for this discussion. Consider now another strain field ε' , solution for an anisotropy ratio $k' > k$. Using it as a trial field for problem (30) with k provides one inequality. Duplicating the argument with k and k' , and $\varepsilon, \varepsilon'$ interchanged, yields after some easy algebra involving (31):

$$SD^{(1)}(\varepsilon_{\perp})^2 \leq \frac{\langle \varepsilon'_{\parallel} \rangle^{(1)} - \langle \varepsilon_{\parallel} \rangle^{(1)}}{(1/k') - (1/k)} \leq SD^{(1)}(\varepsilon'_{\perp})^2, \quad (32)$$

which entails (29) for $k' \rightarrow k$. Thus, the standard deviation $SD^{(1)}(\varepsilon_{\perp})$ of the transverse (PS) component of the strain field increases with k at f fixed, consistently with Table III. Moreover, using (32) and the equality $\partial_k \langle \varepsilon_{\perp}^2 \rangle^{(1)} = -k \partial_k \langle \varepsilon_{\parallel}^2 \rangle^{(1)}$ [from (29)] shows that under SS loading $\langle \varepsilon_{\parallel}^2 \rangle^{(1)}$ is a decreasing function of k . These considerations hold for any fixed microstructure.

Analyzing FFT calculations at $f = 0.1$ for various values of k in log-log plots (not shown), we observe that (for this f) the SDs behave as powers of k with numerical exponents close to $1/4$ or $3/4$: e.g., under SS loading, $SD^{(1)}(\varepsilon_{\perp})$ decays as $k^{3/4}$ when $k \rightarrow 0$, and blows up as $k^{1/4}$ when $k \rightarrow \infty$; meanwhile, $SD^{(1)}(\sigma_{\perp}) = SD^{(1)}(\varepsilon_{\perp})/k \sim k^{-1/4}$ as $k \rightarrow 0$ and $\sim k^{-3/4}$ as $k \rightarrow \infty$. The “soft” case $k \rightarrow 0$ is in agreement with the dilute analytical expressions (33b) and (33c) below, which indicates that the computed systems remained in the dilute regime $f \ll f_r(k) \sim k$. On the other hand, the “hard” case $k \rightarrow \infty$ where strong strain localization takes place (see map C in Table I) is consistent with (33b) and (33c) only if we replace f by $f_r(k) \sim k^{-1}$ in these expressions. Thus,

here, $SD^{(1)}(\varepsilon_{\perp})$ blows up [see (34d)], but behaves as though the system remained in the cross-over regime. This information, extracted numerically, is not contained in the expressions (35d), (38b), for which we could only produce limiting values.

Actually, in the limit $k \rightarrow \infty$, infinite SDs in the *transverse* component of the strain result from its concentration as Dirac lines (see Sec. III B), and are linked to discontinuities (jumps) in its *parallel* component.²⁵ This results in a deformation pattern by a “rigid block sliding” mechanism, the “rigid blocks” being here connected parts of matter separated by discontinuity lines. This block-sliding effect only takes place provided that the strain jump lines have “percolated”. Below “percolation”, sliding is impossible in a linear material and the transverse strain fluctuations described by (33b) strongly increase with k as $SD^{(1)}(\varepsilon_{\perp}) \sim k^{3/4}$. On the contrary, beyond “percolation”, sliding takes place and $SD^{(1)}(\varepsilon_{\perp}) \sim k^{1/4}$ increases in a weaker way, since sliding makes deformation easier. Analogous properties are found under PS loading, provided that k is replaced by $1/k$: e.g., $SD^{(1)}(\varepsilon_{\perp})$ is a decreasing function of k and blows up in the hard loading mode as $\sim k^{-1/4}$ when $k \rightarrow 0$.

Table IV shows numerical results for the strain and stress field averages and SDs, plotted for various anisotropy ratios $k = 0.01, 1$ and 100 . EMA estimates are provided for comparisons. Except when SDs blow up at strong anisotropy, the EMA estimates are in good agreements with FFT results, for porosities up to $f \sim 0.4$. It is worth observing that, in situations of high anisotropy ratios, a change in the structure of the strip patterns in the material coincides with a change of concavity of the standard deviations $SD^{(1)}(\varepsilon_{\parallel})$ of the parallel component of the strain field. For instance, when SS loading is applied at $k \gg 1$, the bands cover the whole medium at $f \approx \pi/8 \approx 0.4$. Around this value, the quantity $SD^{(1)}(\varepsilon_{\parallel})$ changes from a concave to a convex function of f . Such a change also occurs at $f \approx \pi/8$ for the same SDs when $k \gg 1$ and PS loading is applied. FFT field maps then indicate that the structure of the strain pattern also undergoes an abrupt change at this point (with the appearance of thinner strips linking closest neighboring voids – not shown).

2. Standard deviations in the dilute limit

For completeness, we include the standard deviations in the dilute limit (of relevance to nonlinear EMAs) computed from the HS-EMA.

For SS loading, we find for $f \ll f_r(k)$ (low anisotropy or low porosity),

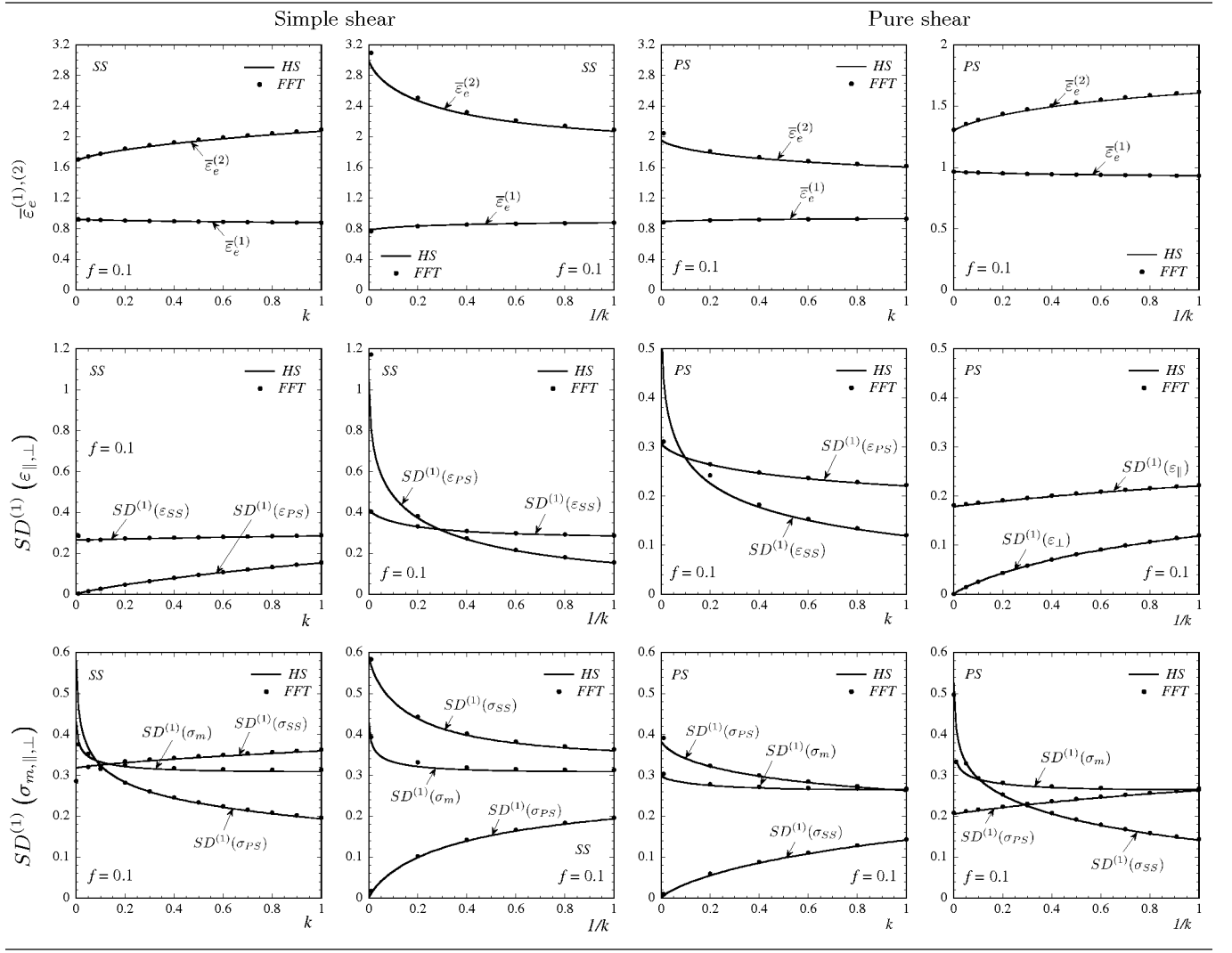
$$SD(\varepsilon_{\parallel}) \sim SD(\sigma_{\parallel}) \sim f^{1/2} k^{1/4}, \quad (33a)$$

$$SD(\varepsilon_{\perp}) \sim f^{1/2} k^{3/4}, \quad (33b)$$

$$SD(\sigma_{\perp}) \sim f^{1/2} k^{-1/4}, \quad (33c)$$

where the $f^{1/2}$ proportionality of the SDs goes along “classical” $O(f)$ dilute corrections to the effective moduli. In limits of infinite anisotropy, where necessarily $f \gg f_r(k) = 0$, the

TABLE III: *SS and PS loadings*. Comparisons between EMA estimates (solid lines) and FFT results (dots) at porosity $f = 0.1$, for averages of the strain along the loading direction in each phase, and standard deviations (SD) of stress and strain components in the matrix, vs. matrix anisotropy ratio $k = \lambda/\mu$. Strains and stresses are normalized by the appropriate macroscopic component in the loading direction (macroscopic strain $\bar{\epsilon} = \langle \epsilon \rangle$, or stress $\bar{\sigma} = \langle \sigma \rangle$). SDs in the voids are irrelevant.



HS estimates provide:

$$SD(\epsilon_{\parallel}) = SD(\sigma_{\parallel}) = \frac{4\sqrt{2}}{\pi^{3/4}\sqrt{3}} f^{3/4} + \left(\frac{64\sqrt{2}}{3\pi^{9/4}\sqrt{3}} - \frac{\sqrt{3}\pi^{3/4}}{4\sqrt{2}} \right) f^{5/4}, \quad k \rightarrow 0, \quad (34a)$$

$$SD(\epsilon_{\perp}) = 0, \quad SD(\sigma_{\perp}) = \infty, \quad k \rightarrow 0, \quad (34b)$$

$$SD(\epsilon_{\parallel}) = SD(\sigma_{\parallel}) = \frac{\pi^{3/4}\sqrt{3}}{29/4} f^{1/4}, \quad k \rightarrow \infty, \quad (34c)$$

$$SD(\epsilon_{\perp}) = \infty, \quad SD(\sigma_{\perp}) = 0, \quad k \rightarrow \infty, \quad (34d)$$

while exact results read:²⁵

$$SD(\epsilon_{\parallel}) = SD(\sigma_{\parallel}) = \frac{4\sqrt{2}}{\sqrt{3}\pi^{3/4}} f^{3/4} + \frac{\sqrt{3}\pi^{3/4}}{8\sqrt{2}} \left(\frac{6}{\pi} + \frac{8}{\pi^2} - 1 \right) f^{5/4}, \quad k \rightarrow 0, \quad (35a)$$

$$SD(\epsilon_{\perp}) = 0, \quad SD(\sigma_{\perp}) = \infty, \quad k \rightarrow 0, \quad (35b)$$

$$SD(\epsilon_{\parallel}) = SD(\sigma_{\parallel}) = (2f/\pi)^{1/4}, \quad k \rightarrow \infty, \quad (35c)$$

$$SD(\epsilon_{\perp}) = \infty, \quad SD(\sigma_{\perp}) = 0, \quad k \rightarrow \infty. \quad (35d)$$

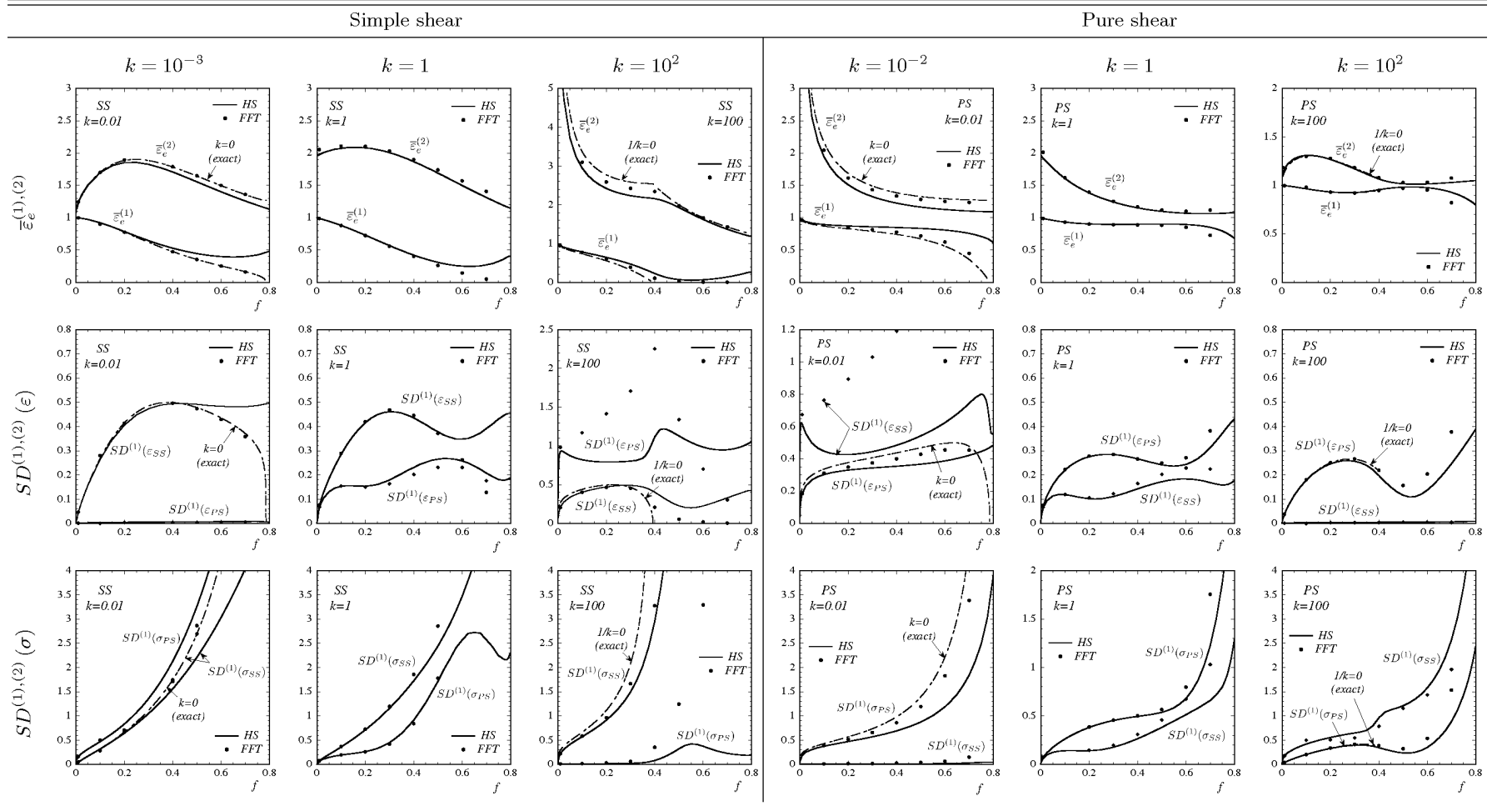
For PS loading, the HS-EMA gives for $f \ll f_r(k)$:

$$SD(\epsilon_{\parallel}) \sim SD(\sigma_{\parallel}) \sim f^{1/2} k^{-1/4}, \quad (36a)$$

$$SD(\epsilon_{\perp}) \sim f^{1/2} k^{-3/4}, \quad (36b)$$

$$SD(\sigma_{\perp}) \sim f^{1/2} k^{1/4}. \quad (36c)$$

TABLE IV: Average shear strains $\bar{\varepsilon}_e^{(\alpha)}$ in the matrix ($\alpha = 1$) and in voids ($\alpha = 2$) vs. porosity f . Comparisons between EMA estimates (solid lines), FFT results (dots) and exact analytical results at $k = 0, \infty$ (dash-dotted lines) for particular values of the matrix anisotropy ratio $k = \lambda/\mu$, in pure shear (PS) and simple shear (SS) loadings. The normalization is the same as for Table III (see legend).



For infinite anisotropy where $f \gg f_r(k) = 0$, the HS estimates provide:

$$SD(\varepsilon_{\parallel}) = SD(\sigma_{\parallel}) = \frac{\pi^{3/4}\sqrt{3}}{4\sqrt{2}}f^{1/4}, \quad k \rightarrow 0, \quad (37a)$$

$$SD(\varepsilon_{\perp}) = \infty, \quad SD(\sigma_{\perp}) = 0, \quad k \rightarrow 0, \quad (37b)$$

$$SD(\varepsilon_{\parallel}) = SD(\sigma_{\parallel}) = \frac{2^{9/4}}{\sqrt{3}\pi^{3/4}}f^{3/4} + \left(\frac{2^{3/4}32}{3^{3/2}\pi^{9/4}} - \frac{\sqrt{3}\pi^{3/4}}{2^{9/4}} \right) f^{5/4}, \quad k \rightarrow \infty, \quad (37c)$$

$$SD(\varepsilon_{\perp}) = 0, \quad SD(\sigma_{\perp}) = \infty, \quad k \rightarrow \infty, \quad (37d)$$

while exact results are:²⁵

$$SD(\varepsilon_{\parallel}) = SD(\sigma_{\parallel}) = (f/\pi)^{1/4}, \quad k \rightarrow 0, \quad (38a)$$

$$SD(\varepsilon_{\perp}) = \infty, \quad SD(\sigma_{\perp}) = 0, \quad k \rightarrow 0, \quad (38b)$$

$$SD(\varepsilon_{\parallel}) = SD(\sigma_{\parallel}) = \frac{2^{9/4}}{\sqrt{3}\pi^{3/4}}f^{3/4} + \frac{\sqrt{3}\pi^{3/4}}{2^{1/4}8} \left(\frac{3}{\pi} + \frac{4}{\pi^2} - 1 \right) f^{5/4}, \quad k \rightarrow \infty, \quad (38c)$$

$$SD(\varepsilon_{\perp}) = 0, \quad SD(\sigma_{\perp}) = \infty, \quad k \rightarrow \infty. \quad (38d)$$

Thus, the HS-EMA correctly reproduces the scaling behavior of the SDs in all cases.

VI. CONCLUDING DISCUSSION

To summarize, we compared the results of the HS-EMA to FFT calculations, and showed that the agreement is excellent, even in the non-trivial case of localizing behavior, as far as effective moduli and averaged fields are concerned, and provided that the void concentration lies below 0.3. This result is relevant to the study of *non-linear* effective-medium techniques: the latter involving both an anisotropic EMA, and a specific self-consistent linearization procedure (which determines the effective anisotropy of the former), the present study shows that should strong deviations between FFT and EMA results in nonlinear media be observed (in the similar set-up of a periodic voided medium, and in similar conditions of porosity and of effective anisotropy), they ought be attributed to the linearization procedure rather than to the underlying liner EMA, even in limits of high effective anisotropy (determined by the field fluctuations in the nonlinear theory). Also, the present work provides a useful independent confirmation of the involved analytical analysis of Ref. 25.

As a by-product of the study, of possible practical applications, we showed that by combining a regular lattice of voids (which makes the structure lighter) and an anisotropic matrix, properties could be tuned so as to make the overall medium elastically isotropic in plane strain.

We also studied analytically the lattice sums which underly the EMA approach, and showed that they possess a scaling

property which, in the dilute limit of small porosity and at high (but finite) anisotropy, allows for a cross-over between regular and singular porosity dependence of the effective medium. A length scale ξ was associated to this scaling, and interpreted as an effective heterogeneity size. It mathematically diverges in the limit of infinite anisotropy. However, its physically associated counterpart being constrained by the finite size of the cell in the periodic medium, cross-over occurs when the effective heterogeneities “percolate”, i.e. when ξ is trivially of order one. This corresponds to a strongly correlated regime of strain localization bands spanning the system.

Actually, scaling properties of lattice sums similar to the one considered here, have already been pointed out by Barber,⁶² elaborating on Hall’s work,⁶³ in a purely mathematical context (in particular, no explanation in terms of length scales was given). Here, we make a connection between this phenomenon and strain localization in anisotropic elastic media. Barber’s paper also provides a means to compute the cross-over function. However, our lattice sums lead to technical difficulties which preclude the straightforward obtention of a similar result, and we leave this issue for future work.

Moreover, we found that under loading in a “hard” direction of the anisotropic medium, standard deviations of the transverse strain component blow up continuously as a power of the anisotropy ratio, as though the system remained in a cross-over regime. This absence of finite threshold for diverging fluctuations, and the above-described behavior, suggest the existence of a special type of continuous phase transition, of infinite order (called a “weak phase transition” by Hall,⁶³), here obviously without symmetry breaking. The presence of logarithmic terms in k (identified numerically in the Appendix) also hints in this direction, since logarithmic corrections to scaling constitute a hallmark of transitions of infinite order.⁶⁴ However, a random version of the system should be investigated before reaching definite conclusions.

Finally, it was observed in Ref. 25 that the singular effective moduli in the limit of infinite anisotropy are directly connected to the hyperbolic character of the governing equations in this limit. The very existence of a cross-over shows without ambiguity that the problem, although elliptic from a strict mathematical point of view, presents a “quasi-hyperbolic” character at short distances for high but finite anisotropy. This observation may be of relevance to theoretical investigations of granular materials, for which a model with a similar anisotropic matrix has been proposed.³⁵

Acknowledgments

The work of M.I.I. and P.P.C. was supported by NSF grant CMS-02-01454. The work of F.W. was supported by a CEA Ph.D. grant. We gratefully thank P. Suquet for having kindly provided to us the notes of Ref. 50.

- * Electronic address: francois.willot@ensmp.fr; Now at: *Centre de Morphologie Mathématique*, 35 rue St-Honoré, F-77305 Fontainebleau Cedex, France.
- † Electronic address: yves-patrick.pellegrini@cea.fr
- ‡ Electronic address: mii23@cam.ac.uk; Now at: Departamento de Aeronáutica, Facultad de Ingeniería, Universidad Nacional de La Plata, Calle 1 y 47, (1900) La Plata, Argentina.
- § Electronic address: ponte@seas.upenn.edu
- ¹ X.C. Zeng, D.J. Bergman, P.M. Hui and D. Stroud, *Phys. Rev. B* **37**, 10 970 (1988).
- ² R. Blumenfeld and D. J. Bergman, *Phys. Rev. B* **40**, 1987 (1989).
- ³ N.C. Kothari, *Phys. Rev. A* **41**, 4486 (1990).
- ⁴ T.K. Ballabh, M. Paul, T.R. Middy and A.N. Basu, *Phys. Rev. B* **45**, 2761 (1992).
- ⁵ P. Ponte Castañeda, G. deBotton and G. Li, *Phys. Rev. B* **46**, 4387 (1992).
- ⁶ P. Ponte Castañeda, *J. Mech. Phys. Solids* **44**, 827 (1996).
- ⁷ P. Ponte Castañeda and P. Suquet, *Adv. Appl. Mech.* **34**, 171 (1998), and references therein.
- ⁸ Y.P. Pellegrini, *Phys. Rev. B* **64**, 134211 (2001).
- ⁹ P. Ponte Castañeda, *Phys. Rev. B* **64**, 214205 (2001).
- ¹⁰ P. Ponte Castañeda, *J. Mech. Phys. Solids* **50**, 737 (2002); *ibid.* **50**, 759 (2002).
- ¹¹ R.F. Bishop, R. Hill and N.F. Mott, *Proc. Phys. Soc.* **57**, 11 (1945).
- ¹² K. Weinberg, A. Mota and M. Ortiz, *Comput. Mech.* **37**, 142 (2006), and references therein.
- ¹³ M. Idiart and P. Ponte Castañeda, *Comptes Rendus Mécanique* **333**, 147 (2005).
- ¹⁴ O. Lopez-Pamies and P. Ponte Castañeda, *J. Mech. Phys. Solids* **54**, 807 (2006); *ibid.* **54**, 831 (2006).
- ¹⁵ L.M. Kachanov, *Fundamentals of the theory of plasticity* (Dover, New York, 2004).
- ¹⁶ For a general survey see, e.g., T.M. Wright, *The physics and mathematics of adiabatic shear bands* (Cambridge University Press, Cambridge, 2002).
- ¹⁷ S. Roux and D. François, *Scripta Metall. Mat.* **25**, 1087 (1991).
- ¹⁸ S. Roux and A. Hansen, *J. Phys. II France* **2**, 1007 (1992).
- ¹⁹ A. Donev, C.E. Musolff and P.M. Duxbury, *J. Phys. A: Math. Gen.* **35**, L327 (2002).
- ²⁰ J. Boksiner and P.L. Leath, *Phys. Rev. E* **67**, 066610 (2003).
- ²¹ L. Benguigui, *Phys. Rev. B* **38**, 7211 (1988).
- ²² D.R.S. Talbot and J.R. Willis, *IMA J. Appl. Math.* **35**, 39 (1985).
- ²³ P. Ponte Castañeda, *J. Mech. Phys. Solids* **39**, 45 (1991).
- ²⁴ P. Suquet, *C. R. Acad. Sci. Paris, Série IIB* **320**, 563 (1995).
- ²⁵ F. Willot, Y.-P. Pellegrini and P. Ponte Castañeda, *J. Mech. Phys. Sol.*, **56**, 1245 (2008).
- ²⁶ S. Torquato, *Random Heterogeneous Materials*, 2nd ed. (Springer, New York, 2005).
- ²⁷ S. Nemat-Nasser and M. Taya, *Quarterly Appl. Math.* **39**, 43 (1981); *ibid.* **43**, 187 (1984) (Erratum).
- ²⁸ K.C. Nunan and J.B. Keller, *J. Mech. Phys. Solids* **32**, 259 (1984).
- ²⁹ Ruibao Tao and Ping Sheng, *J. Acoust. Soc. Am.* **77**, 1651 (1985).
- ³⁰ A. Sangani and W. Lu, *J. Mech. Phys. Sol.* **35**, 1 (1987).
- ³¹ P. Suquet, *C. R. Acad. Sci. Paris Série II*, **311**, 769 (1994).
- ³² D.J. Bergman and K.-J. Dunn, *Phys. Rev. B* **45**, 13262 (1992).
- ³³ R.C. McPhedran and A.B. Movchan, *J. Mech. Phys. Solids* **42**, 711 (1994).
- ³⁴ V.A. Buryachenko, *Int. J. Solids Struct.* **42**, 4811 (2005).
- ³⁵ M. Otto, J.-P. Bouchaud, P. Claudin and J.E.S. Socolar, *Phys. Rev. E* **67**, 031302 (2003).
- ³⁶ D.A.G. Bruggeman, *Ann. Phys. (Leipzig)* **29**, 160 (1937).
- ³⁷ We emphasize however that for periodic lattices in an isotropic medium non-integer powers of f show up at higher orders, see e.g. Refs. 26,30 and R.C. McPhedran and D.R. McKenzie, *Proc. R. Soc. A* **359**, 45 (1978).
- ³⁸ A. Weck, D.S. Wilkinson, H. Toda and E. Maire, *Adv. Eng. Mat.* **8**, 469 (2006); A. Weck, T.H.R. Crawford, A. Borowiec, D.S. Wilkinson and J.S. Preston, *Appl. Phys. A* **86**, 55 (2007).
- ³⁹ M. Idiart, P. Ponte Castañeda, F. Willot and Y.P. Pellegrini, in preparation.
- ⁴⁰ J. Helsing, G.W. Milton and A.B. Movchan, *J. Mech. Phys. Solids* **45**, 565 (1997).
- ⁴¹ J.S. Lormont, *Applications of finite groups* (Dover, New York, 1993).
- ⁴² Specifically, $E = \mu(3 - \mu/\kappa)$, $\nu = (\kappa - \mu)/(2\kappa)$ for plane strain; $E = 4\kappa\mu/(\kappa + \mu)$, $\nu = (\kappa - \mu)/(\kappa + \mu)$ for plane stress; the shear modulus λ of the simple shear mode is unchanged.
- ⁴³ H. Moulinec, P. Suquet, *C. R. Acad. Sci. Paris Série II*, **318**, 1417 (1994).
- ⁴⁴ J. Korrington, *J. Math. Phys.* **14**, 509 (1973).
- ⁴⁵ J.C. Michel, H. Moulinec and P. Suquet, *Comput. Methods. Appl. Mech. Engng.* **172**, 109 (1999).
- ⁴⁶ J.C. Michel, H. Moulinec and P. Suquet, *Int. J. Numer. Meth. Engng.* **52** 139 (2001).
- ⁴⁷ H. Moulinec and P. Suquet, *Physica B* **338** 58 (2003).
- ⁴⁸ J.R. Willis, *J. Mech. Phys. Solids* **25**, 185 (1977).
- ⁴⁹ F. Willot and Y.P. Pellegrini, in *Procs. 11th Symposium on Continuum Models and Discrete Systems, Paris, Jul. 30 - Aug. 3, 2007* (École des Mines, Paris, 2008), in press. arxiv:0802.2488v1 [cond-mat.mtrl-sci].
- ⁵⁰ P. Suquet, *Méthodes de calcul simplifiées pour la détermination des propriétés élastiques de composites à structure périodique*, unpublished notes (1991).
- ⁵¹ More formally, this amounts to using the separable potential approximation, see Y.P. Pellegrini, B. Stout and P. Thibaudeau, *J. Phys.: Condensed Matter* **9**, 177 (1997).
- ⁵² R. Hill, *J. Mech. Phys. Solids* **13**, 89 (1965).
- ⁵³ J.R. Willis, *Adv. Appl. Mech.* **21**, 1 (1981).
- ⁵⁴ A. Hautot, *J. Phys. A: Math. Gen.* **8**, 853 (1975).
- ⁵⁵ Z. Hashin and S. Shtrikman, *J. Mech. Phys. Solids* **11** 127 (1963).
- ⁵⁶ G. Milton and R.V. Kohn, *J. Mech. Phys. Solids* **36**, 597 (1988).
- ⁵⁷ The form is also that of the “Quasi-Crystalline Approximation”, exact here as far as the correlations are concerned. See, e.g., U. Frisch, in *Probabilistic methods in applied mathematics, Vol. I*, A.T. Bharucha-Reid, ed. (Academic Press, New York, 1968), p. 75.
- ⁵⁸ J.E. Gubernatis and J.A. Krumhansl, *J. Appl. Phys.* **46**, 1875 (1975).
- ⁵⁹ T.R. Middy, M. Paul and A.N. Basu, *J. Appl. Phys.* **58**, 4095 (1985).
- ⁶⁰ P. Ponte Castañeda and J.R. Willis, *J. Mech. Phys. Solids* **43**, 1919 (1995).
- ⁶¹ G. Kneer, *Phys. Stat. Sol.* **9**, 825 (1965).
- ⁶² M.N. Barber, *J. Phys. A: Math. Gen.* **10**, 2133 (1977).
- ⁶³ G.L. Hall, *J. Stat. Phys.* **14**, 521 (1973).
- ⁶⁴ M. Weigel and W. Janke, *J. Phys. A: Math. Gen.* **38**, 7067 (2005).
- ⁶⁵ R. Wong, *Asymptotic approximations of integrals* (Academic Press, Boston, 1989).
- ⁶⁶ G.H. Hardy, *Mess. Math.* **49**, 85 (1919).
- ⁶⁷ M.L. Glasser, *J. Math. Phys.* **14**, 409 (1973).

APPENDIX: ASYMPTOTICS OF LATTICE SUMS AND DILUTE LIMITS

We extract the dilute expansions of the lattice sums $S_{\lambda,\mu}$ when $k \rightarrow 0, \infty$ as follows. With the notation

$$A(a, x) = [2J_1(2\pi ax)/x]^2, \quad (\text{A.1})$$

write the lattice sums, with $p = (p_x^2 + p_y^2)^{1/2}$, as

$$S_\lambda = \frac{1}{\pi} \sum_{\substack{p_x \geq 0 \\ p_y \geq 1, p_y \neq p_x}} A(a, p) (p_x^2 - p_y^2)^2 / D(\mathbf{p}), \quad (\text{A.2})$$

$$S_\mu = \frac{1}{\pi} \sum_{\substack{p_x \geq 1 \\ p_y \geq 1}} A(a, p) 4p_x^2 p_y^2 / D(\mathbf{p}), \quad (\text{A.3})$$

where $D(\mathbf{p}) = 4p_x^2 p_y^2 + k(p_x^2 - p_y^2)^2$. The above expressions explicitly acknowledge the fact that the principal diagonal $p_x = p_y$ does not contribute to S_λ , and that the Cartesian axis $p_x = 0$ does not contribute to S_μ . Introducing the lattice sums

$$S_1(a) = \frac{1}{\pi} \sum_{n \geq 1} A(a, n), \quad S_2(a) = \frac{1}{\pi} \sum_{\substack{p_x \geq 0 \\ p_y \geq 1}} A(a, p), \quad (\text{A.4})$$

provides for $k \rightarrow \infty, 0$,

$$kS_\lambda^{k \rightarrow \infty} = \frac{1}{\pi} \sum_{\substack{p_x \geq 0 \\ p_y \geq 1, p_y \neq p_x}} A(a, p) = S_2(a) - \frac{1}{2}S_1(\sqrt{2}a),$$

$$S_\mu^{k \rightarrow 0} = \frac{1}{\pi} \sum_{\substack{p_x \geq 1 \\ p_y \geq 1}} A(a, p) = S_2(a) - S_1(a). \quad (\text{A.5})$$

In $S_\lambda^{k \rightarrow \infty}$ (resp. $S_\mu^{k \rightarrow 0}$) the contribution of the principal diagonal (resp. Cartesian axis $p_x = 0$) has been subtracted from $S_2(a)$. The factors $\sqrt{2}$ and $1/2$ result from n being replaced by $\sqrt{2}n$ on the main diagonal.

One privileged tool for exact asymptotic expansions is the Mellin transform.⁶⁵ The transform and its inverse are defined by:

$$M[f(x); z] = \int_0^\infty dx x^{z-1} f(x),$$

$$f(x) = \frac{1}{2i\pi} \int_{c-i\infty}^{c+i\infty} dz x^{-z} M[f(x); z],$$

where c lies within the analyticity strip (parallel to the imaginary axis) of $M[f(x); z]$ in the z -plane. Shifting the inversion contour to the left encircles the poles on the negative z axis and provides the asymptotic series expansion around $x = 0$ in positive powers of x . Conversely, shifting the contour to the right provides the asymptotic expansion near $x = \infty$ in negative powers of x . The Mellin transform provides, for $0 < c < 3$,

$$A(a, p) = \frac{1}{2i\pi} \int_{c-i\infty}^{c+i\infty} \frac{dz}{(2\pi a)^z} \frac{1}{p^z} \frac{2}{\sqrt{\pi}} \frac{\Gamma(z/2)\Gamma(3/2 - z/2)}{\Gamma(2 - z/2)\Gamma(3 - z/2)}$$

Next appealing to the definition of the Zeta function for $z > 1$, $\zeta(z) = \sum_{n \geq 1} 1/n^z$, and to Hardy's lattice sum^{66,67}

$$\sum_{\substack{p_x \geq 0 \\ p_y \geq 1}} \frac{1}{(p_x^2 + p_y^2)^{z/2}} = \zeta(z/2)\beta(z/2), \quad (z > 2) \quad (\text{A.6})$$

where $\beta(z) = \sum_{n \geq 0} (-1)^n / (2n + 1)$ is the Dirichlet (or Catalan) function,⁶⁷ and interchanging the lattice sums and the contour integral yields:

$$S_1(a) = \frac{-i}{\pi^{5/2}} \int_{c_1 - i\infty}^{c_1 + i\infty} \frac{dz}{(2\pi a)^z} \zeta(z) \frac{\Gamma(z/2)\Gamma(3/2 - z/2)}{\Gamma(2 - z/2)\Gamma(3 - z/2)}, \quad (\text{A.7a})$$

$$S_2(a) = \frac{-i}{\pi^{5/2}} \int_{c_2 - i\infty}^{c_2 + i\infty} \frac{dz}{(2\pi a)^z} \zeta(z/2)\beta(z/2) \times \frac{\Gamma(z/2)\Gamma(3/2 - z/2)}{\Gamma(2 - z/2)\Gamma(3 - z/2)}, \quad (\text{A.7b})$$

where $1 < c_1 < 3$ and where $2 < c_2 < 3$ as the result of the above restrictions. The following properties hold: $\Gamma(z)$ has simple poles at negative integers $z = -k \leq 0$ and has no zeros; $\zeta(z)$ has only one simple pole at $z = 1$, and has (so-called "trivial") zeros at even, nonzero, negative integers; $\beta(z)$ has no poles and has zeros at odd negative integers. Then, by shifting the contour to the left in both integrals, only the poles $z = 1, 0$, contribute to S_1 , and only the poles at $z = 2$ and $z = 0$ contribute to S_2 . Eventually we obtain:

$$S_1(a) = \frac{32}{3\pi} a - 2\pi a^2, \quad (\text{A.8a})$$

$$S_2(a) = 1 - \pi a^2. \quad (\text{A.8b})$$

The polynomial form of these expressions indicates that they are actually *exact*, since for such functions the asymptotic expansion coincides with the function itself.

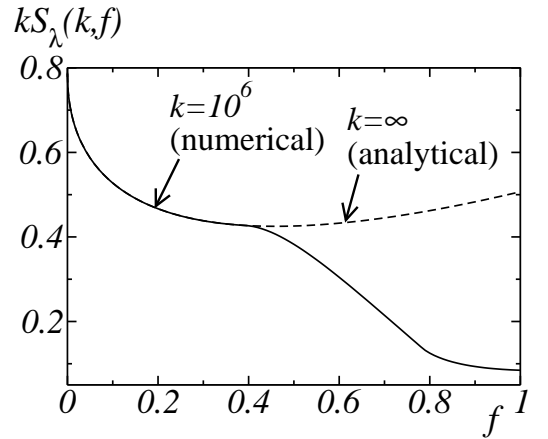


FIG. 7: Quantity $kS_\lambda(k, a)$ vs. void concentration $f = \pi a^2$ as $k \rightarrow \infty$: comparison between (A.9c), dashed line, and a numerical calculation of the lattice sum, solid line, for $k = 10^6$. Breakdown of (A.9c) occurs at $f = \pi/8 \simeq 0.39$.

The validity of (A.8a) is linked to the decay of

$$f(z) = \left| s^{-z} \zeta(z) \frac{\Gamma(z/2)\Gamma(3/2-z/2)}{\Gamma(2-z/2)\Gamma(3-z/2)} \right| \quad \text{as } \Re z \rightarrow -\infty.$$

We have in the limit $f(z) \sim s^{-z} |\zeta(z)\Gamma(z/2)\zeta(z)/\Gamma(-z/2)|$. Owing to the reflection formula

$$\pi^{-z/2} \Gamma(z/2) \zeta(z) = \pi^{-(1-z)/2} \Gamma((1-z)/2) \zeta(1-z),$$

$|\Gamma(z/2)\zeta(z)/\Gamma(-z/2)| \sim \pi^z |\zeta(-z)| \sim \pi^z$. Hence the contribution of the integration line in the limit $c_1 \rightarrow -\infty$ is negligible only if $s < \pi$. In terms of a , this amounts to $a < 1/2$. The breakdown of the obtained expressions thus corresponds to the close-packing limit $a = 1/2$. A similar reasoning using the corresponding reflection formula for $\beta(z)$ provides the same range of validity for S_2 .

Combining (A.5), (A.8) and (19) then results in

$$kS_\lambda^{k \rightarrow 0} = \frac{32}{3\pi} a - 2\pi a^2, \quad (a < 1/2) \quad (\text{A.9a})$$

$$S_\mu^{k \rightarrow 0} = 1 - \frac{32}{3\pi} a + \pi a^2, \quad (a < 1/2) \quad (\text{A.9b})$$

$$kS_\lambda^{k \rightarrow \infty} = 1 - \frac{16\sqrt{2}}{3\pi} a + \pi a^2, \quad (a < \frac{1}{2\sqrt{2}}) \quad (\text{A.9c})$$

$$S_\mu^{k \rightarrow \infty} = \frac{16\sqrt{2}}{3\pi} a - 2\pi a^2, \quad (a < \frac{1}{2\sqrt{2}}). \quad (\text{A.9d})$$

The restrictions $a < 1/2$ and $a < 1/(2\sqrt{2})$ correspond to critical concentrations $f = \pi/4$ and $f = \pi/8$. At these points, either the voids percolate ($k = 0$, PS or SS and $k = \infty$, SS) or the shear bands undertake a configurational change ($k = \infty$, PS).²⁵ An illustration of the breakdown of expression (A.9c) is provided by Fig. 7.

We could not compute analytically the leading corrections in k to these sums. However, by carefully analyzing brute force numerical computations of the sums for k down to 10^{-5} or up to 10^6 for $f = 0.1$, we found that corrections to (A.9a), (A.9b), (A.9c), (A.9d) are of the form $O(k \log k)$, $O(-k \log k)$, $O(k^{-1} \log k)$, $O(-k^{-1} \log k)$, respectively.

As a final remark, we emphasize that only (divergent) asymptotic series for $S_1(a)$, $S_2(a)$ at $a > 1/2$ can be obtained: then, the integrand in both contour integrals blows up as $[z/(4\pi a e)]^z$ where e is Euler's constant. These asymptotic expansions are easily extracted. We do not provide them here since the region $a \gtrsim 1/2$ cannot be examined without appealing to additional investigation procedures (e.g., Padé approximants) which lie outside the scope of this paper.